ABSTRACT

NELSON, NOEL BENJAMIN. Validation and Uncertainty Quantification of a 1x2" NaI Collimated Detector Using Detector Response Functions Created by g03. (Under the direction of Yousry Azmy.)

Detector response functions (DRFs) are relatively new theoretical constructs most useful for inverse analysis of radiation sources and elemental composition. A DRF is formally defined as a function that transforms the incident flux of radiation on a detector into a differential pulse height spectrum or detector response (as measured by a physical detector). Such functions have not yet been derived from first principles of physics, so semi-empirical and Monte Carlo based methods are generally used. One such method, based on semi-empirical modeling and Monte Carlo simulation of photon interactions with a sodium iodide (NaI) detector, is implemented by a code named g03 developed in the Center for Engineering Applications of Radioisotopes (CEAR). g03 has been validated for simple geometries (e.g. centered on-axis sources) with bare (i.e. uncollimated) detectors with 3x3" and 6x6" crystal dimensions. This work uses measurements from three radioactive sources with a 1x2" collimated NaI detector for complex geometries (e.g. off-axis and attenuated sources) to validate the DRF constructed with g03. Three measurement campaigns were performed: on-axis detection of calibration sources, off-axis measurements of a highly enriched uranium disc (HEU) at 41 cm, and on-axis measurements of the HEU disc at 11 cm with steel plates in between to provide attenuation. Simulated responses were created using MCNP computed fluxes folded with a DRF determined via g03. Furthermore, this work quantifies the uncertainty of the Monte Carlo (MC) simulations used in and with g03, as well as the uncertainties associated with each semi-empirical model employed in the full DRF representation. Most of the uncertainties associated with Monte Carlo simulations were controlled by the number of histories run. The uncertainties in the empirical model were determined by either Frequentist or Bayesian methods. In the case of many data points (degree of freedom, DOF, four or higher), direct Frequentist calculation of uncertainty by least squares and parameter derivatives proved more expedient than the Bayesian method (factor of 100 less computation time). However, in cases where fewer measurements were available (DOF less than four), a delayed rejection adaptive Metropolis (DRAM) algorithm was used instead. Overall, the response computed by the DRF for the prediction of the full energy peak region of responses was very good (well within two standard deviations of the experimental response), but tended to overestimate the Compton continuum by about 45-65 % due to physics associated with electron transport in the case of the calibration sources. For the HEU disc measurements, DRF responses tended to significantly underestimate (more than 20%) secondary full energy peaks due to scattering with the detector collimator and aluminum can which is not accounted for in the g03 model of the DRF. Though immediate outside detector scattering is thought to be the main reason for the underestimation, some contribution may also come from unsimulated geometry and uranium

daughter product decay radiation. All of the Monte Carlo uncertainties were constrained to the lowest experimental counting bin (peak channel) relative standard deviation by running a sufficient number of histories. The uncertainties associated with least squares fits to the experimental data tended to have parameter relative standard deviations lower than the peak channel relative standard deviation in most cases and good reduced chi-square values (close to one). However, two fits out of the sixty considered did not meet these criteria: the energy calibration and the Ba-133 Gaussian peak fits for the power law. Fortunately, the energy calibration still proved to be fairly accurate (within 1% of the true incident gamma ray energies) and had a negligible effect on the validation exercise. The other misfit had to be resolved by weighting the power law by the standard deviation of the Gaussian peak standard deviations.

Validation and Uncertainty Quantification of a 1x2" NaI Collimated Detector Using Detector
Response Functions Created by g03

by
Noel Benjamin Nelson

A thesis submitted to the Graduate Faculty of
North Carolina State University
in partial fulfillment of the
requirements for the Degree of
Master of Science

Nuclear Engineering

Raleigh, North Carolina

2014

APPROVED BY:

Robin Gardner	John Mattingly
Ralph Smith	Louise Worrall

Yousry Azmy
Chair of Advisory Committee

DEDICATION

In memory of my dearest and loving mother, Deanna Nelson.

BIOGRAPHY

The author was born in a small town in Oregon called John Day, to parents R. Bryan and Deanna Nelson as the youngest of two children. He graduated from Grant Union High School as the Valedictorian in 2008. He continued his studies at Oregon State University (OSU) for four years in Nuclear Engineering.

At OSU he worked diligently beside his studies as a cook for the university dormitory kitchens and as an undergraduate researcher for the chemistry department. In his chemistry research, he observed the effects of electric voltage, frequency, and amperage on the polymer brush growth of hemoglobin for use in the manufacture of prosthetics. He graduated Summa Cum Laude from Oregon State with an Honors B.S. in nuclear engineering in the summer of 2012.

He continued his graduate studies at North Carolina State University under the direction of Dr. Yousry Azmy. His research includes inverse holdup source characterization methods, and detector response validation and uncertainty quantification.

ACKNOWLEDGEMENTS

TABLE OF CONTENTS

LIST OF TABLES

LIST OF FIGURES

CHAPTER

1

INTRODUCTION

1.1 Research Motivation and Goals

Detector response functions (DRF) have become an area of increasing scientific interest for the last thirty years in several industrial detection applications. These applications include coal spectrometry for composition and location in the interest of mining, oil-well logging, radio-tracing in medicine, computerized tomography (CT) scans, and holdup source characterization. DRF uses could be extended to nuclear safeguards and security applications as well such as border monitoring for illegal transport of radioactive materials, cargo and package monitoring, and unknown source identification at source recovery sites. However, a rigorous mathematical formulation of the DRF has yet to be developed. Therefore, a few working empirical and stochastic approaches have been developed instead to create DRFs.

The concept of a DRF is defined in Section 2.3. For basic purposes a DRF can be considered a function that converts the energy-dependent flux of incoming source particles incident on a detector into a detector response spectrum similar to what is observed in experimental detector measurements. The DRF can also be used in the reverse sense in an inverse problem setting, as a step in the process of predicting the physical characteristics of an unknown source (e.g. holdup problem).

Much of the most recent work on DRFs has been performed by Dr. Robin Gardner and his research group at North Carolina State University. Gardner has developed a fairly accurate DRF model through empirical curve fitting and Monte Carlo analysis. The DRF has been validated against experimental measurements taken by Heath and was found to agree within two standard deviations of the experimental results from Heath. The measurements were taken with 3x3" and 6x6" NaI detectors and Cs-137 sources centered on the detector's front axis at a distance of 10 cm. There was agreement with the Heath benchmark detector measurements of the same sizes up to two standard deviations of the measured Poisson error. [16][4]

Some validation work has been carried out on the source positioned off-axis relative to the detector and with intervening material placed between the source and detector pair. This was done in the interest of developing spectrum analysis software specific to the Compton continuum in order to identify attenuators and account for off-axis geometries. The software that accomplishes this purpose is still under development, but once it reaches fruition it should be considered for incorporation into future works that employ DRFs.

The goal of this work was to use the NaI DRF model developed by Gardner to characterize a NaI 1x2" detector for on-axis geometries, off-axis geometries and attenuated configurations and to validate it against experimental measurements. Also, uncertainty in the model was calculated by Frequentist and Bayesian methods, and compared to measurement and Monte Carlo transport uncertainties. The overarching goal is to incorporate an accurate DRF model into an holdup problem approach to the holdup application to characterize special nuclear material (SNM) deposits at nuclear production and processing facilities.

1.2 Summary of Results and Conclusion

There were three major sets of measurements: on-axis detection of calibration sources, off-axis measurements with a highly enriched uranium (HEU) disc, and the HEU disc with steel plate attenuation between the source and detector. In terms of the calibration source spectra with one or two peaks and a Compton continuum, the computed spectrum predicted the peak well within two standard deviations of the experimental count rate, but overestimated the continuum and valley between the peak and Compton edge. This problem likely came from miscalibration of the electron range multiplier (Equation 2.4) used originally for an uncollimated 3x3" detector, as the same effect was observed in Gardner's original validation work when the multiplier was set too low.

However, this effect did not appear in the two major experimental campaigns involving the HEU disc, as the highest energy peak observed was of too low an energy to create a Compton continuum. The model reproduced the main peak (186 keV) and its shoulder peak (205 keV) well, again within

2

two standard deviations of the measured count rate, but underestimated the convolved peak at (150 keV) and did not reproduce the lead backscatter peak near 100 keV. This was due to scattering with the lead collimator that was unaccounted for by the DRF model, as the model currently only reproduces the effects of scattering within the detector crystal.

Finally, uncertainty quantification of the model took place on every calculated quantity from the flux calculation in MCNP to the Gaussian peak fits for shifting the program. Where the uncertainty was controllable by the number of particle histories chosen in Monte Carlo simulations, it was reduced below the lowest measured uncertainty. Where it was constrained to the accuracy of the model for least squares fitting, the reduced chi-square test was performed to check for goodness of fit.

Two mediocre least squares fits were encountered out of many: the energy calibration and the Ba-133 Gaussian peak fits used for the power law fit. The effects of the energy calibration were found to be inconsequential to the validation results. While the Ba-133 peaks effects on the power law were minimized through a special sum of the least squares weighted by the uncertainties in the Gaussian peak uncertainties (σ^{σ_T}).

CHAPTER

2

REVIEW OF THE LITERATURE

The purpose of this literature review is to lay the foundation for the development of the sodium iodide (NaI) detector response function and the corresponding uncertainty quantification based on the results and discoveries of previous scientists in the field of gamma radiation transport and detection. First, the history and development of the NaI detector and its supplementary equipment will be summarized. Then the major developments in Monte Carlo based transport theory relevant to the construction of DRFs will be discussed. The third section will detail the creation of detector response models. Finally, the last section will concern relevant Bayesian uncertainty quantification methods.

2.1   NaI Detection and Detector Response

Before detector response functions were even considered, detector responses and operation principles had to be developed. The detector of interest in our work is a sodium iodide scintillation detector. Scintillation is simply the emission of a visible photon from a material by dexcitation of an electron following its interaction with incident gamma. The favorable scintillation properties of NaI doped with trace amounts of Thallium (NaI(Tl))were first discovered by Robert Hofstadter in 1948 [20].

Hofstadter concluded that NaI(Tl) would be an efficent detector of ionizing radiation. He determined this based off of the duration of light emission, distribution of light pulses, particle energy discrimination (therefore radioactive source discrimination), and the proportionality of counting events to voltage and amplifier gain. He compared some of these characteristics with another detection material, anthracene, while merely verifying other materials to conclude that NaI(Tl) is a viable detector.

A NaI(Tl) crystal alone does not make a detector. Light emitted from the crystal after an interaction is captured via a photoelectric effect interaction with the photocathode of the detector. The freed electrons are multiplied and amplified into a detectable electronic signal pulse by the photomultiplier tube (PMT). The first photmultiplier tube was developed by Harley Iams and Bernard Salzberg much earlier than Hofstadter, in 1935. [6]

They observed the amplification of the primary photocurrent (a stream of electrons) through the effects of secondary emission and the photoelectric effect. Secondary emission is when an electron current strikes a charged plate and releases more electrons than were absorbed by the plate. Iams and Salzberg found that their photomultiplier tube was superior to gas phototubes as they had no interference at high audio frequencies from small fluctuations in its current supply, while still comparable to the vacuum phototubes (other detector PMT candidates). This model is the basis for modern PMT's.

The small electronic output signal from the PMT is then amplified and reshaped from a sharp edged pulse into a wider pulse (based on the difference between a rising and falling exponential) for easy processing. This wider pulse is passed to the multichannel analyzer (MCA), which outputs a differential pulse height spectrum (DPHS) also known as a detector response. A DPHS is created simply by setting a small pulse amplitude window to count pulses of varying heights within the window within a counting period between two energies called a channel. An MCA does this for hundreds of channels at once across the entire detector's energy range. The detector's energy range is determined partially by size and pulse amplitude gain settings. Low energy photons are resolved better by higher gain and the inverse is true for high energy photons. Also, large detectors have better interaction cross sections with higher energy gammas.

The first MCA was invented by George Kelly at Oak Ridge National Laboratories (ORNL) in 1953. Kelly prized his method as being much faster than older methods using single channel analyzers and more reliable with channel width and position errors meeting statistical standards set at the time. [7] Since then MCAs and pulse processing equipment have become more efficient and compact, such that they are often combined together into one machine that is controlled by local desktop software.

Figure 2.1 summarizes and illustrates the whole basic NaI detection process. For further details

of the detection process and pulse processing equipment, please refer to KNOLL's book on Radiation Detection and Measurement.
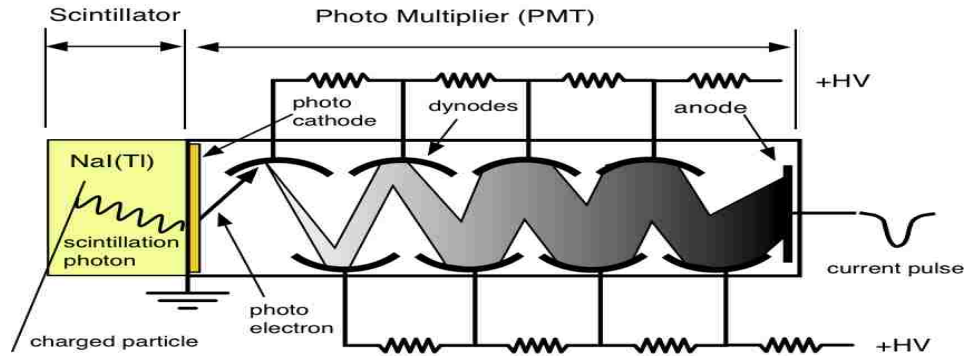
Figure 2.1 A basic NaI detector schematic. [14]

In most cases, the current pulse is sent to the pulse processing equipment and MCA to convert the small collection of electrons from the PMT into a response spectrum. Detector response spectra can be used to locate and identify sources of gamma radiation since the response peak channel is proportional to the incident energy of the incident radiation. It is proportional because the relationship between the energy deposited by radiation in the NaI crystal to the scintillation light yield is fairly linear for energies above 100 keV. A quadratic energy calibration using at least three known sources can account for the slight nonproportionality of detector channel to energy, and thereby be used to identify the energy of the incident radiation from other unknown sources.

In this case, detector response measurements of known sources will be validated against synthetic responses for attenuated and off-axis geometries. A typical detector response spectrum for a small detector is shown in Figure 2.2.
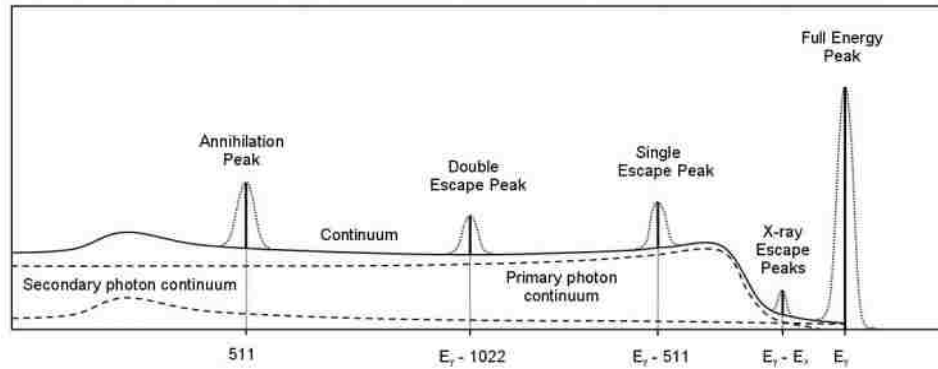
Figure 2.2 Predicted detector response spectrum of a medium sized detector with labeled regions of interest [15]

Every section of the response spectrum is the result of a combination of one or more photon interactions with the detector crystal or its casing material. The three major types of photon interactions with matter include: photoelectric effect, Compton scatter, and pair production. The photoelectric effect occurs when a photon is absorbed by an atom, and a bound electron is then expelled from that atom. Compton scatter occurs when a photon is merely deflected by an atom, and thereby loses a fraction of its energy and changes direction. The third interaction occurs when a high energy photon (greater than 1.022 MeV) interacts with the nuclear electromagnetic field and creates an electron-positron pair that are propelled in opposing directions. Further details of basic particle interactions can be found in Hubbell's report on Photon Cross Sections. [5]

Knoll's book mentions several spectral components that appear in a typical response spectrum as a result of the three basic particle interactions. These include the full energy peak, Compton continuum, and the several other types of peaks that appear in Figure 2.2.

The full energy peak of the spectrum is produced by a combination of all three basic gamma particle interactions with the detector crystal resulting in full energy deposition. Ideally, the full-energy peak would be a straight vertical line, but due to the finite energy resolution of a detector, the spectrum is blurred or spread to a Gaussian profile centered around the true peak channel, or energy. The sources of the spread can be usually attributed to statistical fluctuations in the total number of information carriers (scintillation photons for scintillators) created during a given detection event. Other reasons include electronic noise (radio signals, other electronic equipment, etc.), variations in the active detector volume (ie. defects, nonuniformity), and changes in operating parameters during measurements. In an investigation to validate a Monte Carlo calculated NaI detector response, a good representation for NaI energy resolution was measured to vary inversely (improve) with

7

increasing incident particle energy. For most measurements it varies from 8-15%. [17]

The continuum is created by the probable set of energy depositions from Compton scatter at various angles of deflection with incomplete energy deposition in the detector crystal. The continuum can also be affected by Compton scattering outside of the detector where the deflected photon is detected instead of the electron that is freed when the scatter occurs in the detector crystal. One example is a backscatter peak where the photon scatters at a 180° angle from the rear detector wall into the detector crystal. [9] The shape of the continuum and backscatter peaks can also be significantly affected if an attenuator is in placed front of the source, or if the source is off-axis affecting the number of photons that scatter off of the detector casing into the crystal at a given energy. It is useful in many applications to be able to match different continuum shapes to their most probable cause.

Escape peaks arise when pair production occurs in the detector crystal, but one (single) or both (double) the photons that are created from the annihilation of the resulting positron escape. These events typically occur in small detectors near the edge of the crystal where it is easy for electrons to escape the crystal. When the positron-electron pair is created, the original photon loses the amount of energy required to create the mass of an electron and a positron. The rest mass of both an electron and a positron are approximately 511 keV. The electron created will not contribute much to the response, but the positron does once it annihilates with another electron. The annihilation event creates two photons equivalent to the lost rest mass of each particle, 511 keV, which travel in opposite directions. If both photons escape frequently without depositing energy in the detector crystal, then a double escape will appear in the spectrum at the energy of the incident gamma minus two times the electron rest mass ($E_o - 1.022MeV$). If only one of the photons deposit their energy in the crystal frequently, then a single escape peak will appear in the spectrum at the original incident gamma energy minus one electron rest mass ($E_o - 0.511MeV$).

An annihilation peak is observed when pair production occurs in the detector shielding, or alternatively in the source shielding, and one of the 0.511 MeV photons created in the following positron annihilation event is detected. Finally, characteristic X-rays (usually $E_{X-ray} < 100keV$) are created from the de-excitation of atoms that were involved in a photoelectric event with an incident photon. Typically, the emitted X-rays is reabsorbed by the detector medium and contributes to the full energy peak. However, if the detector is fairly small and these X-rays escape, then an X-ray escape peak is observed in the response slightly below the full-energy peak ($E_o - E_{X-ray}$).

Any detector can produce a response, but NaI(Tl) scintillators are some of the most commonly used in practice. This is because they are cheap and fairly easy to manufacture in varying sizes, have fairly high light emission among scintillators, have high scintillation efficiency (heavy material Z=53) and fairly linear radiative energy deposited to light yield. The two major weaknesses of

NaI(Tl) detectors are their large decay times between pulses and fairly low energy resolution (wide full-energy peaks).

Decay time simply refers to the amount of time it takes for the ionized electrons from a detection event to decay from an excited state at the Thallium activator sites back to the ground state and produce scintillation photons for the detector pulse. Subsequent incident gamma rays cannot be detected during this decay time. For NaI(Tl), the decay time is 230 ns, which is much slower than an organic scintillator which have typial decay times around 2 ns. Therefore, organic scintillators are preferred for fast counting experiments where spectral information is less important than timing.

Knoll defines Energy resolution as $R = \frac{FWHM}{H_o}$ where $FWHM$ is the full width at half the maximum of the full energy peak and H_o is the height of the peak at its center. Therefore, a lower resolution means the peak is narrower compared to its height and requires fewer channels to define the peak (better for distinguishing peaks that are close together in energy). Because FWHM is energy dependent and dependent on the statistical fluctuation in a given measurement, for a given detector type the Poisson limit of the resolution is defined as $R|_{Poisson limit} = 2.35/\sqrt{N}$, where N is the total number of information carriers. For NaI detectors, the theoretical limit would be about 1.2%, since it produces around N=38,000 information carriers (scintillation photons), whereas a semiconductor detector with $N = 10^5 - 10^6$ has a much lower limit of about 2.25%. NaI does not approach this limit closely though, as their is further loss of those scintillation photons from emission to absorption in the photocathode.

However, NaI(Tl) is the best scintillation detector for spectroscopy applications (not fast pulse timing experiments) because it has one of the highest photon absorption to light yield of 38,000 photons/MeV. Only CsI(Tl) and Cs(Na) are higher with 65,000 and 39,000 photons/MeV respectively. Cs(Na) has pretty equivalent properties to NaI, but has a much slower decay time between pulses. Additionally, CsI(Tl) has a bad emission wavelength (540 nm) that doesn't couple well with standard PMTs absorption spectrum (400-450 nm). Due to these weaknesses, generally NaI(Tl) is preferred among scintillators. [9]

For fine measurement applications in the lab, however, a semiconductor detector made of high purity Germanium (HPGe) is usually preferred. It has better resolution overall ranging from 0.13-1%. [21] So, the full-energy peaks of the HPGe would be at least ten times thinner than a NaI peak at the same energy. However, the major weaknesses of HPGe are that it requires cryogenic cooling, it is difficult to manufacture in large sizes, and it is generally expensive. Therefore, for field work (e.g. uranium holdup measurements), NaI(Tl) detectors are generally used due to their greater affordability and portability. Field application is the goal of this work, plus continuum effects are more important than peak resolution for determining source strength and location. Hence, a 1x2" NaI(Tl) scintillation detector was chosen to conduct the validation exercise reported here.

2.2 Monte Carlo Based Radiation Transport

Detector responses can be predicted mathematically by taking the product of the detector's response function (DRF) with the flux (particle speed per volume) of the radiation incident on the detector [9]. The particle flux can be predicted from the solution of the Boltzmann transport equation at the location of the detector crystal due to a given source. The equation was first derived by Ludwig Boltzmann in 1872. [8] Since then, many approximate methods have been developed for solving the Boltzmann equation under certain assumptions suitable for a variety of applications.

One of the more popular transport methods is the Monte Carlo method. The Monte Carlo method does not solve the transport equation itself, instead it simulates the particles and their trajectories through the modeled materials using sequences of pseudo-random numbers. Then it determines the average state of the physical system from the average behavior of the particles. [13] The software chosen for these calculations is the Monte Carlo Neutron-Particle (MCNP) transport code. It was created formally in 1977, though its roots extend back to the late 1940s, at the dawn of the nuclear age. This section outlines the basics of MC transport for calculating incident flux on the detector for the purpose of validating the DRF.

First, particles are simulated and transported according to Boltzmann physics within the volume of interest. Instead of solving the transport explicitly for the entire volume to obtain the flux, the fluence is calculated inside the detector volume only. The fluence, Φ, is defined as

$$\Phi = \lim_{\Delta V \to 0} [\frac{\sum_i s_i}{\Delta V}]. \tag{2.1}$$

If a large number of particles were simulated, this quantity could be calculated directly. [10] Simply by tracking particles through a cell of interest and summing up all of the particle tracks within the very small discrete spheres, the flux is approximated. For large volumes like nuclear power reactors this method becomes inefficient and less accurate. For small detector volumes, however, it works quite well. [2]

That is how Monte Carlo simulation works by simulating moving particles directly and tracking them through simulated media. Particle tracks from birth in a source to death (absorption or escape) from the system including all intervening scatters are called histories. The number of particle histories (N) executed in an MCNP run is chosen in order to obtain the desired level of uncertainty in the calculated quantities.

A typical particle history proceeds as follows. First, particles are initialized with random location, energy, and direction of motion according to a defined source distribution. Particles then interact or pass through the specified media according to well defined, material dependent, probability

distributions called cross sections. A photon microscopic cross section, $\sigma_{reactiontype}$ is defined as the probability of a photon-nuclear reaction with a nucleus. [1] It can also be thought of as the effective cross sectional area presented by the nucleus to the beam of incident photons, and cross sections have units of cm^2. Cross sections depend on energy, material, and interaction type.

Often microscopic cross sections are multiplied by the atom density of the medium to make a macroscopic cross section. Photon macroscopic cross sections, $\mu_{interaction}$, (also called attenuation coefficients) are simply the probability of a certain interaction with the medium occurring per unit path length traveled. [1] Summing the macroscopic cross sections of every interaction type yields the total attenuation cross section, μ. There are several minor interaction cross sections (Raleigh scattering, Thompson scattering, etc.), but the largest contributions for photons come from the three aforementioned interactions: photoelectric effect, Compton scatter, and pair production.

If these interactions produce secondary particles, they too are stored and tracked as new histories after the original particles terminate. Finally, after each particle history has been recorded, the particle track (s_i) through the detector volume is added to the running tally calculating the flux according to the average of Equation (1) piece by piece until all the histories are tallied.

The Monte Carlo transport method is very effective and simple, but can be inefficient and have high variances if variance reduction techniques are not applied. Variance in Monte Carlo is based on the number of histories run, so the simplest way to reduce variance in such a calculation is to run more particle histories. Sometimes this is not feasible (rare events), therefore variance reduction techniques are used instead. In Exploring Monte Carlo Methods by Dunn and Shultis the most common variance techniques are described, which include particle weighting, truncation, splitting, and Russian roulette.

The first method is called weighting. A biased multiplier (called a weight) may be applied to particles undergoing desired physical events in order to force rare interactions to occur more often without running as large numbers of histories. The biased particles' contribution to the tally (the score) is then renormalized by mulitplying by $1/weight$. This ensures that desired events are well sampled, but the tally still represents an unbiased system.

Further subtypes of this technique include importance sampling, and implicit absorption. In importance sampling a particle's contribution to the tally may be taken as the product of the particle's weight and the probability of the occurrence of the event of interest. The probability density function (PDF) that describes this event may be adjusted to an alternate simpler PDF, as long as a multiplicative correction factor is applied to the weight equivalent to the original PDF divided by the alternate PDF. When optimum adjoint transport solutions are applied, the variance can theoretically be reduced to zero. Similarly, alternate PDFs may also be used to force interactions or affect the distance between collisions.

For implicit absorption, particles are never allowed to be killed by absorption. Instead, every time an absorption event would occur, the particle's weight is reduced by multiplying its weight by the probability of survival $(1 - \frac{\mu_a}{\mu})$. Then a particle interaction is chosen for the particle from the remaining non-absorption interaction probabilities. Therefore, in this scenario, a particle may only be killed by leaking out of the system. To prevent buildup of low weight particles in the system, this technique is usually paired with the Russian roulette technique.

Truncation methods set cutoff limits for when a particle should be terminated. For example, if a particle reaches a position outside of the system of interest (leakage), then tracking would be terminated. Other examples, include unfavorable directions, low energies, and low weights unlikely to contribute much to the tally of interest. Truncation helps to kill particles early that are only wasting computational resources.

Finally, splitting and Russian roulette schemes are almost always applied together. Splitting occurs when a particle enters a region designated of higher importance and interest (e.g. the cell where a tally is calculated, and it is split into m particles. Each particle weight is then given by a 1/m fraction of the weight of the original particle. Russian roulette is exactly the opposite of splitting. Particles that travel into regions of low interest may be killed by random selection. Some 1/m fraction of particles are killed, and the remainder increased in weight by a factor of m. [2]

All of the variance reduction techniques reduce variance without biasing the tallies, if used correctly. Often these techniques increase computational efficiency and decrease computation times. Many production Monte Carlo transport codes apply some of these techniques automatically, while allowing the others to be chosen as options.

In this work, the Los Alamos National Laboratories (LANL) code Monte Carlo Neutron Transport code (MCNP) was used to compute flux tallies incident on the 1x2" NaI detector model. The code was originally implemented for neutron transport, but can also be used for other particle transport, such as photon transport. Monte Carlo based calculation was also used in part to calculate the DRF.

2.3 Detector Response Functions

The DRF ($R(E, h)$) is defined as the probability that a photon incident on the detector with energy E will give rise to a pulse with height h. [18] DRFs are useful for converting flux to counting spectra, calculating detector efficiencies, and also for the reverse, transforming responses back into flux. The latter purpose will be explored more in future research, but in this work focus will remain on the former purpose.

At the present, no fully physical model exists to describe DRFs, but there are several stochastic (MC) and empirical models. Gardner's NaI DRF model is one that combines empirical relations with

Monte Carlo simulation. Gardner's original work with his colleague Avneet Sood validated 3x3 NaI synthetic detector responses to the Heath benchmark Cs-137 spectrum. Gardner's model was found to be more efficient (required far less particle histories for accurate calculation) and was shown to match better with the Heath experiments than MCNP's F8 response tally. [16] It was chosen for our work for these reasons and also because MCNP simulates responses according to direct energy deposition in the detector crystal. It generates no DRF, and a DRF will be needed for future holdup work.

The Heath experiments were performed on a 3x3" NaI detector in 1964 as a benchmark for a number of gamma sources. All measurements were very high fidelity. The measurements were performed in a lead shielded box to reduce background radiation and all spectra were counted well over 10,000 counts in the peak channel for less than 1% counting uncertainty. For further information, see Heath's Gamma Ray Spectrum Catalogue. [4]

Gardner's model generates a DRF for a desired detector size, source distance, and source energy (single peak), through the following set of steps. First, Gardner's model takes into account the nonlinear dependence of NaI scintillation efficiency ($\frac{scintillation\ light\ yield}{energy\ deposited}$) on the energy deposited in the detector by the incident photon. As mentioned before (section 2.1), the nonlinearity in scintillation efficiency is an inherent property of NaI(Tl) crystals, and it is particularly pronounced at energies below 100 keV. However, this nonlinearity is still significant for all incident energies below 3 MeV. Gardner used the following nonlinear empirical relationship (from fits to experimental data) to calculate scintillation efficiency for his DRF

$$S(E_e) = 1 + k_1 exp[-(ln\ E_e - k_2)^2/k_3],$$

$$E_e \geq 10\ keV,$$

$$S(E_e) = 1 + k_1 exp[-(ln\ E_e - k_2)^2/k_4], \tag{2.2}$$

$$E_e \leq 10\ keV,$$

where E_e is electron energy in keV. k_1 is 0.245, and k_2 is $ln\ 10 = 2.30258$. k_3 is 7.1635, and k_4 is 5.1946. The electrons are the very same electrons that are involved in interactions with photons incident on the detector crystal. The second step involves Monte Carlo particle transport simulation in which each scattered electron that deposits energy in the detector is multiplied by the scintillation efficiency (Equation 2.2) at the energy deposited. [16]

The Monte Carlo calculation is conducted with Peplow's code called DRFNCS. It simulates several hundred detector response spectra through Monte Carlo transport where photon interactions are forced in the detector, but leakage of secondary particles is allowed producing the continuum of

the spectra. Only about 100,000 particle histories are necessary to produce results with uncertainty under 1%, whereas MCNP F8 Gaussian energy broadened (GEB) spectra require on the order of billions of particles to produce the same precision. The difference typically saves about a day in computation time.

Next, the peaks were stripped from the response spectra so that each contiuum could be processed alone. Principle component analysis (PCA) was performed on the correlated response variables and the covariance matrix to produce a small set of uncorrelated variables (principal components). The principal components and the mean vector were stored as data and can reproduce accurate continuum easily when multiplied with the desired channels vector.Essentially, the continuum can be recalled quickly without the need to be regenerated by Monte Carlo simulation for each DRF generated.

So, when a new DRF needs to be generated, the algorithm need only to generate the full-energy peak of interest by Monte Carlo transport simulation and adds this contribution to the continuum to produce the desired DRF. [22] The modified version of Peplow's code (adjusted by the nonlinear scintillation efficiency) is called g03. The code is in the process of being updated and is proprietary to the Center for Engineering Applications of Radioisotopes (CEAR).

Finally, the Monte Carlo simulation of g03 is modified by several empirical equations to correct pieces of the spectra that are not simulated fully by the Monte Carlo calculation. The g03 DRF peak section is spread according to the following power law (Equation (2.3))

$$\sigma_T(E_I) = a E_I^b, \tag{2.3}$$

where a and b are empirical fit parameters, and E_I is the energy of the incident gamma ray. This law is simply an empirical relation that comes from a Least Squares fit of the standard deviations of experimentally measured full-energy peak responses produced by the detector of interest. [16]

The flat Compton continuum of the DRF is produced by various empirical fits of entire experimental responses (not only the peaks). This is necessary because there is as of yet, some undiscovered phenomena causing a higher magnitude of the continuum than predicted by current physics models and data. Simple Compton scatter and pair production physics and partial energy deposition due to electron or photon leakage through the detector walls can predict the shape of the Compton continuum but underestimates its magnitude. A normalization factor was developed to account for this effect called the electron range multiplier, since the effect causing the underestimation of the continuum was believed to be connected to the electron range. The empirical relation is given by Equation 2.4

$$R_e = 1 + A_1 exp(-A_2 E_I) + A_3 exp(-A_4 E_I) \tag{2.4}$$

$$A_1 = 39.662, \; A_2 = 3.4052, \; A_3 = 1.5434, \; A_4 = 0.1576,$$

where E_I is the energy of the incident photon, and $A_1 - A_4$ are parameters fit from experimental responses. This factor is a pseudo-electron range equation designed to correct the magnitude of the synthetic Compton continuum produced by the Gardner's DRF. It was fit through trial and error for 3x3" NaI detectors and may not apply to the detector of interest in this work (1x2" NaI detector). [23]

Responses, thus, may be measured or calculated. Validation of Gardner's model has already been completed on some levels, but almost no uncertainty quantification of the model has been performed. The primary goal of this work is to conduct a validation exercise of the DRF for a specific NaI detector of interest and account for its uncertainties.

2.4 Uncertainty Quantification

In the process of comparing measured to computational model results there are three types of uncertainty in practice. There is measurement uncertainty, model uncertainty, and numerical (simulation) uncertainty. Quantifying uncertainty is important in determining the precision of the model and the computed results. The more precise a result is, the more likely it can be reproduced, and the higher the level of confidence in the applicability of the computational model.

Measurement uncertainty for detection and counting was found to follow a Poisson distribution for a single measurement. This is because the decay of a nucleus is a binary process. It either decays or it does not. The chance of decay per unit time is constant and rather small for a large number of nuclei and a short measurement time (compared to the nuclide's half-life). A binomial distribution under these conditions (constant and small probability of success) will reduce to a Poisson distribution. [9]

In a Poisson distribution the variance is equal to the mean (the number of counts). Therefore, the variance of the measurement is equal to the mean number of counts. In a single measurement this would be the number of counts measured in a detector channel. The standard deviation is then simply the square root of this count, and the fractional standard deviation (relative to the total count) is one divided by the root of the count.

To then extend this measurement uncertainty to count rates and net counts (gross count - background count), one simply uses propagation of uncertainty. Anytime a basic operation (addition, subtraction, multiplication, or division) is performed on the measured count, likewise a transformation must be made to the variance of the counts. If the variables involved (e.g. counts and time) are

independent of one another, then a general formula exists for calculating total uncertainty of the final quantity (Equation 2.5)

$$\sigma_u^2 = (\frac{\partial u}{\partial x})^2 \sigma_x^2 + (\frac{\partial u}{\partial y})^2 \sigma_y^2 + (\frac{\partial u}{\partial z})^2 \sigma_z^2 + /ldots,$$

(2.5)

where $u = u(x, y, z, \ldots)$ is the quantity derived from basic quantities $(x, y, z, \ldots)$ with known variances $(\sigma_{variable}^2)$. The formula is useful for determining the associated uncertainties of many quantities (e.g. count rates and net counts) for various purposes, such as those used in the reduced chi-square test described near the end of this section. [9]

It turns out that simulation uncertainty for Monte Carlo transport calculation is very similar to that of measurement uncertainty. This is due to the fact that the particles themselves are being simulated and tracked as a psuedo-random process. Measurement standard deviation is equivalent to the square root of the number of counts (the mean) in a channel. So it makes sense that the Monte Carlo standard deviation is simply the square root of the number of particle histories in a tally bin. The fractional standard deviation is simply equivalent to the reciprical of the standard deviation. [2]

Determination of the model parameter uncertainty is a more difficult task. For this purpose, there are two major statistical methods to choose from: Bayesian and Frequentist Theory. Since the core of Frequentist Theory requires a large number of data points, a Bayesian method was naturally chosen for the power law Gaussian fits, power law, and the energy calibration fits. Whereas Freqentist methods were chosen for the normal Gaussian fits for shifting spectra and the Gaussian fits of the peaks of experimental spectra for the energy calibration due to the abundance of channels in the peaks of those spectra and for efficient calculation.

Smith's book, Uncertainty Quantification, describes Frequentist and Bayesian statistics quite well. In both methods, parameter means of each relationship were found via the method of nonlinear least squares. This method solves for the mean parameter values that produced the lowest value of the L_2 norm (sum of the squares) of the error. Frequentist methods treat these values as the parameter means and subsequently calculates a Chi squared and covariance matrix to determine the parameter uncertainties. Bayesian methods only use the means for an initial guess (priori information). Further details of least squares methods can typically be found in advanced linear algebra texts. With parameter derivatives and error variance, the Chi squared and covariance matrices can be calculated.

First, however, the error variance must be calculated from the residuals. The error variance is defined as follows

$$\sigma^2 = \frac{1}{n-p} R^T R$$

(2.6)

where R is the residual vector of the differences between the model evaluated at the means predicted

by least squares and the experimental data ($R = Y_{experimental} - f_{model}(q)$). Also, n is the number of parameters, and p is the number of model parameters. Next the χ matrix can be calculated as simply the derivative of the model with respect to each parameter, k at each data point i ($\chi_{ik}(q) = \frac{\partial f_i(q)}{\partial q_k}$). Using the square of the χ matrix and the error variance the covariance matrix can simply be defined as

$$V = \sigma^2 [\chi^T(q)\chi(q)]^{-1}. \tag{2.7}$$

The covariance matrix contains each parameter variance along its diagonal. Simply take the square root of the diagonal values to find the parameter standard deviations. The Frequentist method is very accurate and quick to calculate for cases where there are many more experimental data points than the number of parameters. However, when confidence in a fit is lower due to fewer data points, Bayesian codes fair better. [11]

Bayes theorem expressed in words simply states that parameters are random variables with associated probabilistic densities that make use of known information or new information obtained from conducted measurements. This method picks the best posterior density that reflects the distribution of parameter values based on sampled observations. In other words it finds the probability density functions (pdfs) of model parameters that maximizes the likelihood function. Further details of the likelihood function and Bayesian theory are given in Smith's Book or his reference D. Calvetti and E. Somersalo, Introduction to Bayesian Scientific Computing.

DRAM was used to calculate Bayesian model parameter uncertainties. From Haario's article "DRAM: Efficient adaptive MCMC" one learns that DRAM stands for Delayed Rejection Adaptive Metropolis algorithm. In this work it is used to estimate the most likely means of the model of interests parameters to verify those determined by least squares fits by employing Monte Carlo random sampling of the parameter values, called chains. DRAM also determines the uncertainty in the parameters from the direct statistical variations in the parameter chains.

The basis of DRAM comes from the Random Walk Metropolis algorithm (RWM). RWM comes from Monte Carlo principles and is fairly easy to implement. First, the variance is obtained in the same way that the error variance is typically calculated: from the sum of the square of the residuals divided by the number of degrees of freedom (Equation 2.6). Second, the covariance is estimated from the inverse of the χ squared distribution which come from partial parameter derivatives of the model (as defined by Equation 2.7). A Choleski factorization of the covariance matrix is formed. Lastly, with the factored matrix, the parameters are varied in a semi-random way with psuedo-random numbers chosen from a set of different distributions. Based on likelihoods of randomly chosen parameter values the algorithm either chooses to accept (if the likelihood is increased) or possibly reject and the rejection probability increases every time the likelihood function decreases.

Using regular statistical methods, again the parameter standard deviations can be estimated from the chains of random parameter values.

DRAM works along the same principles, except that the rejection condition is augmented with a more advanced algorithm that increases the probability of acceptance (promoting mixing or broader exploration of the chains). Also, DRAM adapts by suggesting a Gaussian proposal distribution centered at each chain position and retrieves more information about the posterior using it to update the covariance matrix. Together these advancements make a much more efficient algorithm than basic RWM. [19]

Additionally, both Frequentist and Bayesian methods give estimates of the model parameters that best reproduce a curve along the measured data points. Sometimes, least squares fits and maximum likelihood estimates can produce poor curve fits. So, from Bevington and Robinson's Data Reduction and Error Analysis, one can obtain two useful tools for model examination: the reduced chi-square test and linear correlation coefficients.

The reduced chi-square test helps to provide a quantified measurement of the goodness of fit. The definition of the reduced chi-square is shown by Equation 2.8.

$$\chi^2 = \sum_{j=1}^{n} \frac{[h(x_j) - y(x_j)]^2}{\sigma_j(h)^2}$$

$$\chi_v^2 = \chi^2 / v, \tag{2.8}$$

where n is the total number of data points. $h(x_j)$ is the measurement, and $y(x_j)$ is the model solution at data point j. Also, $\sigma_j(h)^2$ is the variance in the measurement at data point j, and v is the number of degrees of freedom ($v = n - p$) where p is the number of parameters. In our work, the variance will likely be the poisson variance for a simple count spectrum, or the propagated uncertainty for net counts and count rates. A reduced chi-square test will produce a value equal to one for an ideal case, however, it is generally considered to be still a good fit for values less than ten. Values less than one simply mean that the spectrum was overfit, and may have required a simpler model or fewer data points to produce a similar result.

Furthermore, in the event of a poor fit, the model can be examined more closely by examining the linear correlation coefficients. The linear correlation coefficient matrix can be calculated as follows (Equation 2.9):

$$\rho_{jk} = \frac{\sigma_{jk}^2}{\sigma_j \sigma_k} \tag{2.9}$$

where σ_{jk} is the covariance at row i and column j as calculated by Equation 2.7, and σ_j and σ_k

are the diagonal standard deviations of the parameters from the covariance matrix (σ_{jj} and σ_{kk}). The linear correlation coefficients of a model can reveal a weak parameter in the model that might not be contributing much to the model fit. Parameters with many correlation coefficients under 0.2 should be considered for removal or substitution. [3]

CHAPTER

$$3$$

EXPERIMENTAL SETUP AND COMPUTATIONAL MODEL

This section will detail the experimental setup and the Monte Carlo computational transport models used to simulate the experiment's geometric configuration and calculate the flux incident on the detector. A detector description will also be provided, as well as how the detector intrinsic efficiency was calculated. The Monte Carlo calculated quantities are necessary for calculating response spectra for comparison against those obtained via experimental measurements with the actual detector.

3.1 Experimental Setup

The entire experimental campaign was designed and performed at the Safeguards Laboratory at Oak Ridge National Laboratory. The initial campaign was completed over the course of a couple of weeks in June of 2013. Further measurements (such as those for the power law fit) were taken on various days over the course of the spring of 2014, courtesy of ORNL personnel. All sources and detection equipment were provided by ORNL. Each measurement was taken with the same detector, detection equipment, and settings.

The detector of interest for validation of Gardner's DRF model is a 1 inch diameter by 2 inches

height right cylinder EFC Model 1X2P collimated NaI detector. This small detector is one used in uranium holdup experiments at ORNL and is an example of a detector used for field measurements of holdup within the holdup measurement system, HMS. A schematic of the detector is shown in Figure 3.1.

ITEM NO.	PART	Material
1	Case	Aluminum
2	Plug	Aluminum
3	Electronic Housing	Void
4	Rear Shield	Lead
5	Polymer plate	Plastic
6	Steel Enclosure	Stainless Steel
7	PMT	Void
8	Crystal	NaI
9	Tin Shield	Tin
10	Collimator	Lead
11	Collimator Front	Lead
12	Front Cap	Aluminum

SECTION E-E

DETAIL F
SCALE 2 : 1

TITLE:

ORNL 1x2" NaI Detector

SIZE **A** DWG. NO. NAIDET REV

SCALE: 1:2.5   WEIGHT: SHEET 1 OF 1

Figure 3.1 A schematic detailing the 1x2" NaI detector used at ORNL.

As can be seen, the detector is well shielded with lead except on the front face where the collimator aperture allows radiation into the detector from a limited extent of directions covering the corresponding fraction of the unit sphere. Hence, the detector has approximately a 45 degree in-axial-plane angle of vision from the center of its circular front. Contributions to the detector response from any source of radiation far enough off of the axis of the cylindrical detector will be significantly attenuated and radiation incident on the side or rear of the detector will not likely contribute to the measured response spectrum (except for very high energy photons that are not sufficiently attenuated by the detector's lead collimator). The rest of the detector components are fairly standard. It has a PMT, an aluminum sheath (container), etc., as shown in the detector schematic, Fig. 3.1.

Overall, measurements were taken far away from the walls on a table with at most a aluminum tee in the setup. Scattering off of the plastic table, walls, and floor were very unlikely since there is a high probability for interaction of gamma-ray photons with high Z materials. The tee included a small scattering possibility, but it was considered negligible. Therefore, the room geometry and the aluminum tee were not simulated. Only the source, detector, and the air in between were simulated.

In the first set of experiments, a source was placed at a set distance from the detector center (on-axis). The source was held in place on a ring stand, or taped to the front of the detector (for quick counts). The source was typically a button calibration source with known activity and dimensions. These measurements were performed for base validation, energy calibration of the detector, and power law fitting for the DRF.

The parameters of all of the calibration sources used for validation are listed in Table 3.1. Details of the sources used for the energy calibration and the power law fit are not reported here, as these measurements were only intended for determining detector properties.

Table 3.1 Dimensions and activities of calibration sources used for experimental measurements

Source	A.R. (cm)	Thick. (cm)	Act. (μCi)	Created	Measured	Act. Meas. (μCi)
Cs-137	0.25	0.318	5.01	9/28/2005	2/20/2014	4.13 ± 0.62
Co-60	0.25	0.318	0.8516	3/1/2002	6/21/2013	0.1927 ± 0.029

Note: All calibration sources used in this work were created by Eckert and Ziegler, and the active source dimensions (active radius, A.R., and thickness) used in the MCNP model were taken from the Type D disc model in the catalog. Furthermore, according to the supplier "Sources are manufactured with contained activity (Act.) values of ±15% of the requested activity value unless otherwise noted in the catalog." [27]

Note that only the active volume of these sources was simulated in MCNP and not the plastic

case surrounding them, since attenuation was assumed to be negligible. The emission energies and relative intensities of the gamma-rays of interest for each source used are tabulated in Table 3.2.

Table 3.2 Gamma ray energies and relative intensities of all sources measured were taken from Brookhaven National Laboratory's Nudat2.6 database. [28] Unlisted uncertainties were assumed to be one in the last digit.

Source	Peak No.	Energy (keV)	Relative Intensity (%)
Am-241	1	59.5409(1)	35.9(4)
U-235	1	105.0(1)	2.00(3)[*]
U-235	2	109.0(1)	2.16(13)[*]
U-235	3	143.76(2)	10.96(14)
U-235	4	163.356(3)	5.08(6)
U-235	5	185.715(5)	57.0(6)
U-235	6	202.12(1)	1.080(23)
U-235	7	205.316(10)	5.02(6)
Ba-133	1	80.9979(11)	35.6(3)[*]
Ba-133	2	356.0129(7)	62.05(1)
Cs-137	1	661.657(3)	85.10(20)
Mn-54	1	834.848(3)	99.9760(10)
Na-22	1	1274.537(7)	99.941(14)
Co-60	1	1173.228(3)	99.85(3)
Co-60	2	1332.492(4)	99.9825(6)

[*]Note: gamma-rays from the same source that were within 1 keV of each other were averaged and their intensities summed together.

The next set of experiments focused on the source of interest (uranium-235 or U-235) and were specifically conducted for the DRF validation exercise. Since it is very unlikely that a detector will be directly pointed at a holdup material deposit when the deposit has an unknown location, strength, and shape, off-axis detector spectra are of great interest in the holdup field. This is also necessary for holdup configurations where the source is distributed and thus contributes to the response of a stationary detector from broad angles of incidence. So, a source was affixed to an aluminum tee and prepared specifically for accurate off-axis measurements.

The detector was placed on the center steel bar while the source was put on the crossbar held by a vice and a steel ring holder at a distance of 38 cm from the detector face (41 cm from the front face of the detector crystal). The source was then moved laterally left and right of center, or the axially aligned position, in 5 cm intervals up to 20 cm. Measurements ceased at 20 cm because the source

started to become indistinguishable from background beyond that distance. For visual reference, a photograph of the lateral off-axis experimental setup is shown in Figure 3.2.
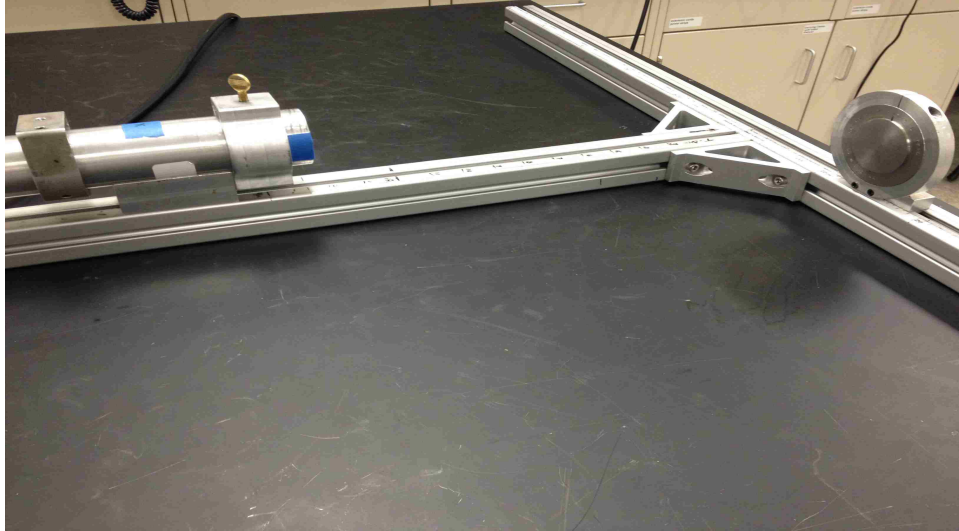
Figure 3.2 Photograph of the HEU disc off-axis experiment 41 cm from the detector and 15 cm to the right (x=+15cm).

The source was a highly enriched uranium (HEU) disc source of known activity, dimensions, and enrichment. The dimensions of the U-235 source are given in Figure 3.3.
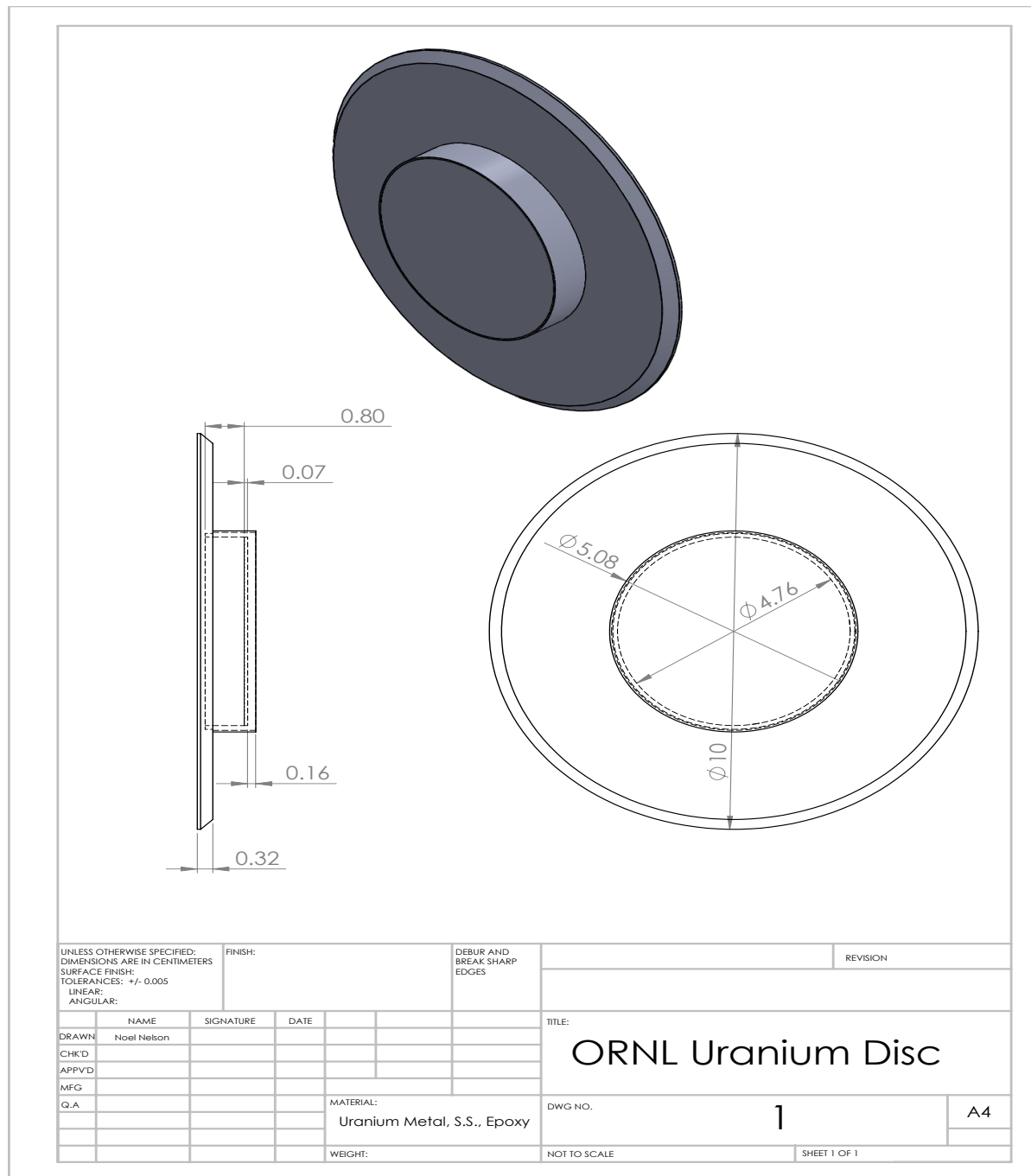
Figure 3.3 Dimensions of the HEU disc as prescribed from ORNL. The disc is made of stainless steel (shell), epoxy (adhesive), and HEU (4.76x0.07cm active source area).

The source in the disc is composed of U_3O_8, uranium's naturally occurring chemical form. The uranium compound is set on polyethylene epoxy and encased in stainless steel. The activity of the disc was 736 μ Ci on December 1, 2004. However, since uranium-235 has a very long half life (703.8 million years for U-235), the activity of the source at the time of the measurement was similar to its initial activity. The individual uranium nuclides that comprise the disc source employed in our experimental campaign are listed in Table 3.3.

Table 3.3 Enrichment of the uranium disc source

Nuclide	Weight %
U-234	1.016
U-235	93.162
U-236	0.400
U-238	5.421
C (natural)	1.009E-3

The disc is of a high enrichment of U-235. U-235 is a common target material for holdup problems in the nuclear fuel production industry because holdup material deposits present a proliferation risk and can become a criticality safety concern. The typical holdup measurement in this case will seek to detect the naturally emitted low energy gamma radiation. Hence, the focus of the validation experiments has been on the low energies of the detector spectrum where the highest intensity (most probable) gamma rays of U-235 are emitted (140-190 keV). This also explains the choice of the smaller NaI detector size, as high energy detection that would necessitate larger detectors to improve detection efficiency is of lower interest in the holdup field.

The last set of experiments were also performed on the highly enriched uranium disc but with a few modifications. First, one or two steel plates taped to the front of the NaI detector to provide attenuation. Second, the lateral distance between detector and source was reduced from 38 cm to 8 cm (11 cm from the crystal), and finally only on-axis measurements were taken. These measurements simulated the attenuation that would be provided by steel pipe and equipment walls that normally stand between the detector and a holdup material deposit. The dimensions of the first steel plate were 105.22mm x 157.75mm ($\pm 0.02 mm$) with a thickness of 0.86 $\pm 0.04 mm$. The second plate was 101.62mm x 152.66mm ($\pm 0.02 mm$) and 0.90 $\pm 0.02 mm$. For visual reference, a photograph of the HEU attenuation experiment at 11 cm is shown in Figure 3.4.
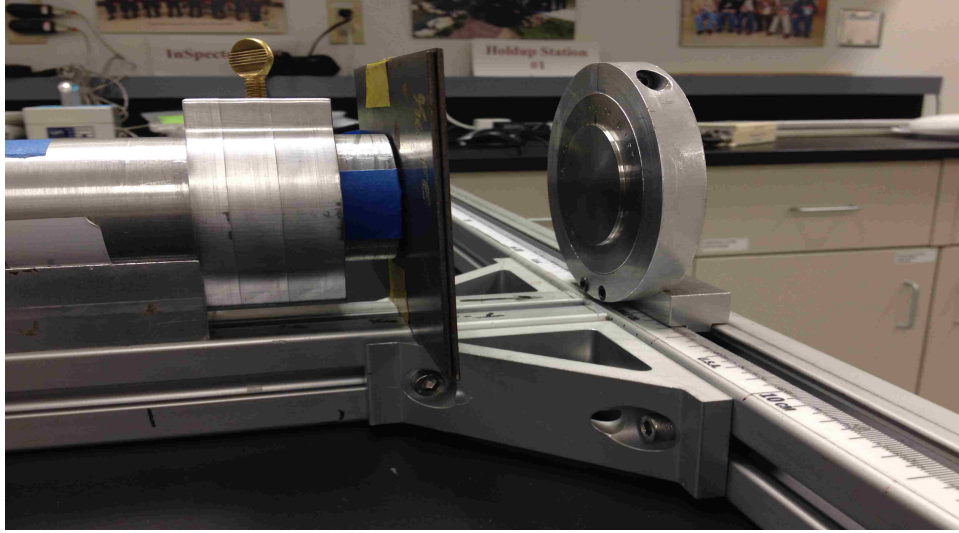
Figure 3.4 Photograph of the HEU disc attenuation experiment with two stainless steel plates attached to the detector (11 cm from the source).

For simplicity, in the MCNP simulation the isotopic compositions of the stainless steel plates were kept the same as the steel used to encase the detector and to encase the HEU source. The weight percent of each elemental isotope used in the steel alloy is listed in Table 3.4.

Table 3.4 Stainless steel alloy composition used in the MCNP simulations.

Nuclide	Weight %
Cr-50	0.800
Cr-52	16.2
Cr-53	0.200
Cr-54	0.400
Mn-55	2.00
Fe-54	4.20
Fe-56	64.8
Fe-57	1.50
Fe48	0.200
Ni-58	6.60
Ni-60	2.50
Ni-61	0.100
Ni-62	0.300
Ni-64	0.100

This composition of steel was taken directly from the MCNP model created by ORNL. The original model is available upon request from the Safeguards & Security Technology Group at ORNL.

3.2 Monte Carlo Transport Models

Version five of the Monte Carlo (MC) code MCNP (Monte Carlo N-Partical Transport Code) was used to calculate the incident gamma-ray photon flux on the 1x2 NaI detector crystal. MCNP is a radiation transport code developed by Los Alamos National Laboratory (LANL) that simulates a large number of random particle histories (particle tracks through a medium as well as collisions with its nuclei) in a user specified geometric configuration according to specified material cross sections (taken from the Evaluated Nuclear Data Files, ENDF). On the order of a few billion particle histories were run for each flux calculation to keep the MC statistical errors smaller than the measurement uncertainties.

The computational geometry specified for MCNP was simplified from the actual experimental geometric setups described in Sec. 3.1. Instead of including all details (i.e. objects) within the room, only the detector and all of its components and the source were simulated within a sphere of air. Only immediately adjacent objects like the table, the aluminum tee, and source holding

apparatuses would be likely to contribute in a small way to the collided fluence tally. There would be no contribution to the uncollided fluence tally as at least one Compton scatter with one of these objects would be required before the particle struck the detector. The detector collimator reduces the likelihood of these events further by reducing the detector solid angle by which particles can strike the detector crystal. So, the secondary geometry (table, tee, etc.) would only make a small contribution to the Compton continuum portion of detector spectra and hence was excluded from the MC models.

With the simplified geometry, an F4 (average fluence) tally was taken in the detector crystal cell by MCNP. MCNP calculates the fluence in a manner very similar to the fluence definition given by Equation 2.1, by summing the particle track lengths over the given cell volume for each discrete energy bin as specified by the user. In our case, 512 equal and discrete energy bins were chosen to match the energy range given by the DRF, and to match the 512 channels observed in the measured spectra. The average fluence tally over cell volume V was approximated discretely as follows,

$$\bar{\Phi}_V(E) \simeq \frac{1}{NV\Delta E} \sum_{i=1}^{N} \sum_{j=1}^{n_i} W_i^j s_i^j \, [\frac{1}{cm^2}], \tag{3.1}$$

where n_i is the number of times the ith particle enters V at energy E_k within energy bin k, s_i^j is that particle's jth track length in V, and W_i^j is the particle's weight when entering V for the jth time. Also, N is the total number of histories simulated by MCNP, and ΔE is the width of the tally's energy bin centered at energy E. This relation is only an approximation of the average fluence, but if a large number of particle histories pass through the cell volume, then it is a fairly accurate tally. [2]

However, as the MCNP fluence is based on the total number of particle histories, it can be converted to a flux as follows

$$\bar{\phi}(E) = \bar{\Phi}_V(E) \cdot A\gamma \, [\frac{photons}{cm^2 \cdot sec \cdot MeV}] \tag{3.2}$$

where A is the activity of the source in Becquerels (Bq) or decays/sec, and γ is the yield in particles/decay. So simply multiplying the F4 tally (fluence) by the source activity and yield converts the tally to the approximate scalar flux effective over the volume of the detector crystal.

Again, the detector response can be predicted by multiplying the DRF by the incident flux. However, Gardner's DRF does not fully include a direct property of specific NaI detectors, absolute efficiency, so it must be considered in the formal definition (Equation 3.3). [24] A differential pulse height spectrum (detector response), dN/dH is defined as

$$\frac{dN}{dH} = \int R(H,E)S(E)dE \approx \sum_{i=1}^{G} R_G(H,E_i)\bar{\phi}(E_i)\epsilon_{abs}(E_i). \tag{3.3}$$

The formal definition from Knoll is listed first and is approximated by the more directly applicable second definition. R(H,E) is the differential probability that a quanta of energy within dE about E leads to a pulse with amplitude within dH about H (DRF). S(E)dE is the differential number of incident radiation quanta with energy within dE about E. [9] $R_G(H,E_i)$ is Gardner's DRF, which is the differential probability that a flux of energy E_i leads to a pulse with amplitude within dH about H (DRF), and $\epsilon_{abs}(E_i)$ is the absolute efficiency. $\bar{\phi}(E_i)$ is the flux. To fully determine a detector response using Gardner's model, a new quantity must be defined and calculated: absolute efficiency.

Detector efficiency in general determines the percentage of radiation particles detected to the number emitted. There are two main classes of detector efficiency, absolute efficiency and intrinsic efficiency. Knoll defines absolute efficiency as simply the ratio of the number of detector pulses recorded to the number of particles with energy E emitted from the source. Absolute efficiency is dependent mainly on detector properties (cross-sections) and the counting geometry (source to detector position). Whereas the intrinsic efficiency is the ratio of the number of detector pulses recorded to the number of radiation quanta incident on the detector. The intrinsic efficiency is accounted for by the DRF, however, the absolute efficiency is not. Therefore it must be approximated as the energy deposited along the average path length through the detector crystal in MCNP simulation. [9]

In other words, the total absolute efficiency is the probability of particles incident on the detector interacting with the detector crystal over all energies (thereby creating a pulse at energy E). This probability is defined as

$$\epsilon_{abs}^{j}(E) = P_{interaction} = 1 - e^{-\mu_{tot}(E)\cdot s_j(E)} \tag{3.4}$$

where $\mu_{tot}(E \to E', \Omega \to \Omega')$ is the NaI photon macroscopic cross section and probability that an incident particle of energy E interacts per unit path length. $s_j(E)$ is the track length and an MCNP program called ptrac was used to record a large number of possible particle track lengths. This distribution was then averaged over all track lengths to produce an average absolute efficiency $\bar{\epsilon}_{abs}(E)$ as shown in Equation 3.5.

$$\bar{\epsilon}_{abs}(E) = \frac{1}{N_t} \sum_{j=1}^{N_t} \epsilon_{abs}^{j}(E) \tag{3.5}$$

N_t is the total number of track lengths recorded by ptrac. Again, the absolute efficiency is

multiplied by the DRF and the incident flux to produce a response spectrum (Equation 3.3). However, since Gardner's model typically underestimates the flat continuum under the response due to electron physics concerning channeling or possibly NaI impurities the resulting computed response must be normalized to the experimental response. [16] In our work, the normalization factors (the ratio of the areas under each curve) necessary to pull up the computed response to the experimental were found to be between two and eighteen. This is in good agreement with Gardner and Sood's results as they had experimental measurements that were up to around an order of magnitude greater than the responses predicted by g03.

CHAPTER

4

VALIDATION

Overall, the simulated detector responses predicted by Gardner's model predicted the highest intensity peak region of the experimental spectra fairly well, but had some difficulty in the continuum and secondary peak regions. In the highest intensity peak region of the response, most of the computed spectrum lay within two standard deviations of the experimental spectrum's centroid. The continuum discrepancies between the predicted and measured responses in the calibration sources appear to stem from miscalibration of the electron range multiplier (Equation 2.4) for the collimated 1x2" NaI detector. Gardner's current model was validated only for larger bare NaI detectors and not for collimated detectors and therefore some differences were expected. Whereas, significant underestimation of the secondary peaks occurred in the highly enriched uranium (HEU) disc spectra most likely due to outside crystal scattering with the detector collimator and other components.

4.1   Cs-137 Measurement

The first measurement was of a Cs-137 source. The Cs-137 source measurement was taken at a distance of 10 cm from the center of the detector face with the calibration source described by Table 3.1. The high source activity ($4.13\ \mu Ci$) allowed for for a precise measurement with less than one

percent uncertainty in the peak region in terms of counts (according to Poisson counting statistics), and it was counted for 4000 seconds. This source was used for validation and as one of the data points for the power law fit but not for the final energy calibration. The resulting spectra computed and measured are given in Figure 4.1a and compared with the computed response without the lead collimator and aluminum sheath simulated in the MCNP flux calculation (Figure 4.1b).

(a)   **(b)**
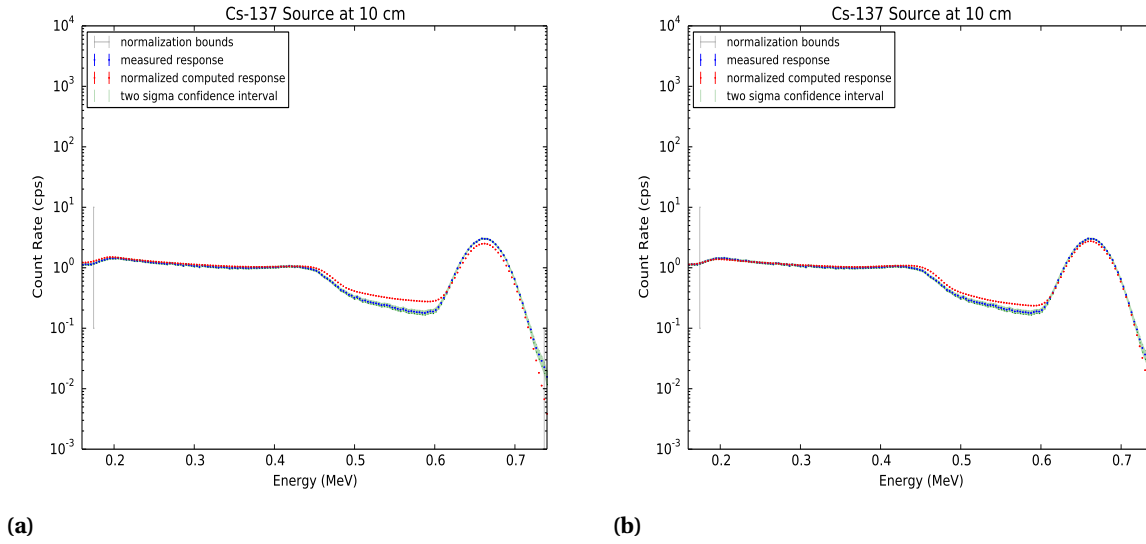
Figure 4.1 Measured and normalized computed responses for the Cs-137 calibration source at 10 cm (normalized across bounds) with aluminum can (a) and without aluminum can and collimator (b).

It is apparent that the backscatter peak is overestimated and the peak underestimated. However, the greatest difference lies in the area between Compton edge and the peak, which will henceforth be referred to the valley of the response. At first this effect was thought to be just a product of the model being unable to account for the collimator geometry. In Sood's PhD thesis, a similar problem was occurring in the valley region of the response for their NaI 3x3" detector. However, the effect was reversed. For a bare NaI crystal simulation in MCNP for the flux calculation, the resulting response underestimated the valley. Simulating the detector aluminum sheath or can corrected this underestimation. [12]

In that manner, the same effect is observed here. Taking away the collimator and aluminum sheath from the MCNP geometry resulted in a response with a lower valley. This means that the collimator and can geometry were not the source of the shallow valley discrepancy.

Another difference between this validation exercise and Gardner and Sood's validation exercises, was how the computed spectrum was normalized to the measured response. Gardner and Sood chose to normalize to the peak channel only, whereas in this work, normalization to the area under the section of interest bounded by the normalization bounds was chosen instead. The normalization factor used to normalize the computed to the measured response spectrum is described mathematically by Equation 4.1

$$A_c = \sum_{n_{b1}}^{n_{b2}} R_i^c,$$

$$A_m = \sum_{n_{b1}}^{n_{b2}} R_i^m,$$

$$N_f = \frac{A_m}{A_c}, \tag{4.1}$$

where R_i^c is the computed count rate, and R_i^m is the measured count rate at channel i. n_{b1} and n_{b2} are the normalization bounds. Normalization bounds were chosen on a case by case basis. In this case the bounds were chosen to avoid bins artificially augmented by the rebinning process and unnecessary noise after the full energy peaks. Rebinning was accomplished by assuming the count rates within the old bins were uniformly distributed, and then collecting them into the new bins according to the fractions of the old bins determined by the uniform pdf. All contribution from the negative energy bins created from the energy calibration were lumped into the first two bins by the rebinning algorithm. Therefore those two bins were not included in the normalization.

The main reason for the normalization according to sections was chosen to minimize the effects of response error in parts of the spectrum. The other reason was to avoid choosing between multiple peaks in a spectrum. However, in this case normalizing to the peak channel revealed the true source of the valley problem as shown by the renormalized spectrum in Figure 4.2a and Gardner's responses resulting from various electron range multipliers: Figure 4.2b.

(a)

(b)
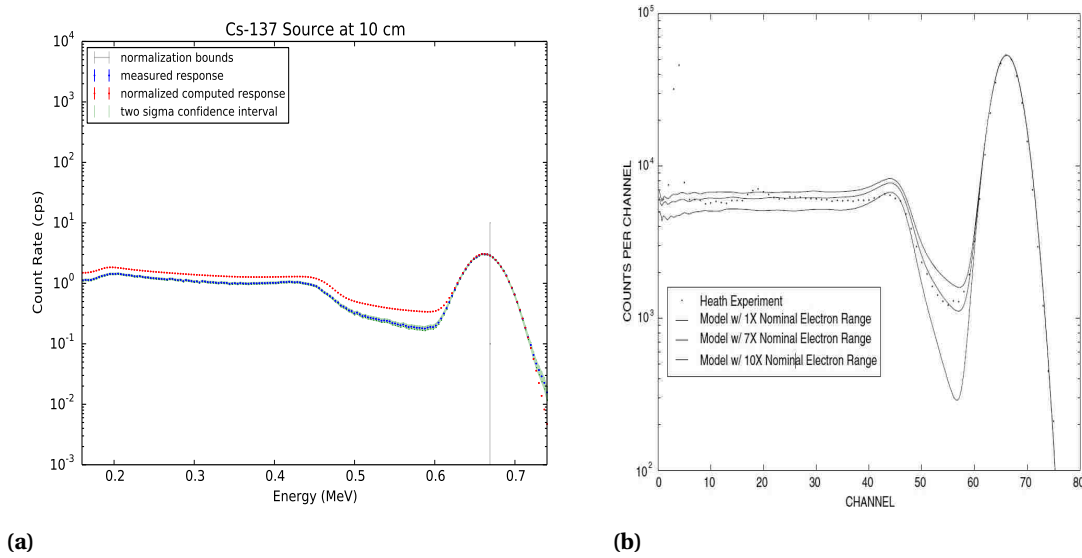
Figure 4.2 (a) Measured and normalized computed responses for the Cs-137 calibration source at 10 cm (normalized to the peak). (b) 3x3" NaI detector computed responses over a varying electron range multiplier compared with the measured response from the Heath benchmark.

Now, as can be seen, the whole response spectrum is overestimated to the left of the peak for the figure on the left. A similar effect is observed by a spectrum with an electron range factor that is too low in Gardner's figure (right). [16] A range multiplier that is too high underestimates the continuum and a valley, while the reverse is true for one that is too low. Since the size of the detector and number of channels of the 1x2" ORNL detector is very different from Gardner's detector it is not surprising that the value of the electron range multiplier may no longer be optimal. Furthermore, the psuedo-electron range multiplier (Equation 2.4) was fit for Gardner's detector by trial and error. For this reason, and the fact that the HEU spectrum of interest contains far less contribution from Compton scatter, the correction of the factor is reserved for future work.

4.2 Co-60 Measurement

The next measurement concerned the Co-60 source described in Table 3.1 taped directly to the detector face. The low source activity (0.1927 μCi) required 1600 seconds for a reasonable number of counts (400 counts, 5% Poisson uncertainty) even on the detector face, so no further measurements were taken with this source. However, this source was only used for the detector energy calibration

and a simple baseline validation (shown in Figure 4.3a). The energy calibration and its parameter uncertainties are discussed further in Section 5.2.

**(a)**   **(b)**
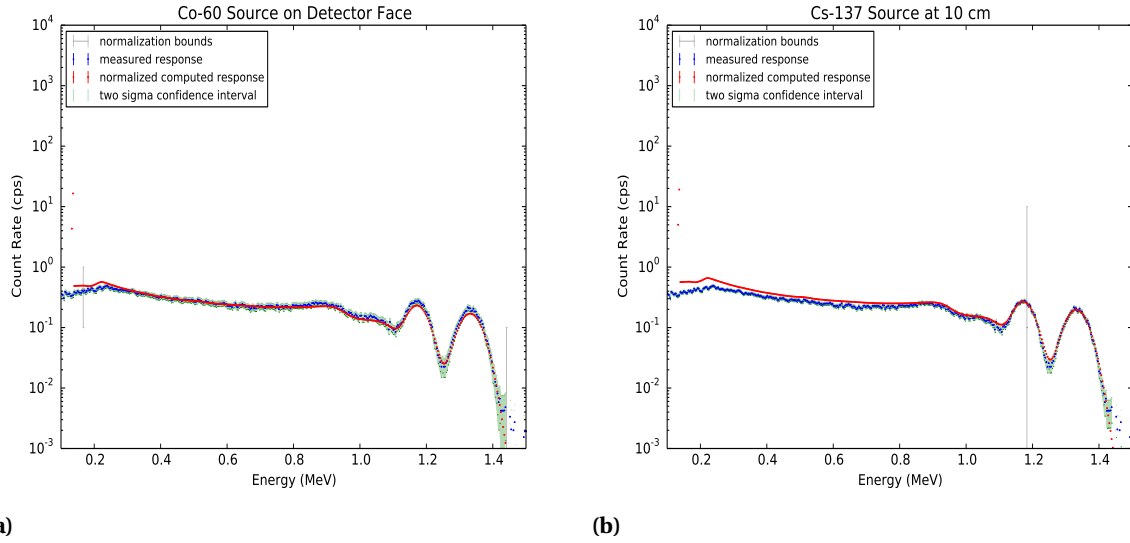
Figure 4.3 (a) Measured and normalized computed responses for the Co-60 calibration source on the detector face using normalization across a range of channels (a) and normalized to the highest intensity peak (b).

As expected, the measured spectrum shows some significant fluctuation in the confidence interval along the response due to the low number of counts (higher uncertainty). The normalized computed response stays mostly well within the confidence interval of the measured response except at the backscatter peak around 2 MeV and the peaks are slightly underestimated. The two Compton edges and most of the continuum are predicted fairly well, however the backscatter peak region around 0.2 MeV is overestimated and the full energy peaks are slightly underestimated.

The overestimation may appear to be less significant in this case due to wider confidence bounds (from the lower fidelity of the measurement), but it is still apparent on closer inspection. The cause is most likely the same as the Cs-137 case, miscalibration of the electron range fit in the g03 source code. Normalization bounds were chosen for the same reasons as the Cs case.

4.3   Axial HEU Disc Measurement Set

The first set of HEU disc measurements were performed in order to test the performance of the DRF model for off-axis geometry. All measurements were carried out at a distance of 41 cm on-axis (y direction) from the crystal (38 cm from the face) and in set increments of 5 cm in the x direction. The central and first two positions used a 400 s background count, whereas the last two positions (x=15,20 cm) used background count times equivalent to the measurement count times. All background count times were chosen based on propagation of the net count uncertainty.

The HEU disc source at the central position (x=0 cm) was counted for four hundred seconds. The normalized computed and measured responses are given by Figure 4.4. The HEU disc specifications and composition can be found along with further details of the source geometry for the entire measurement set in Section 3.1.
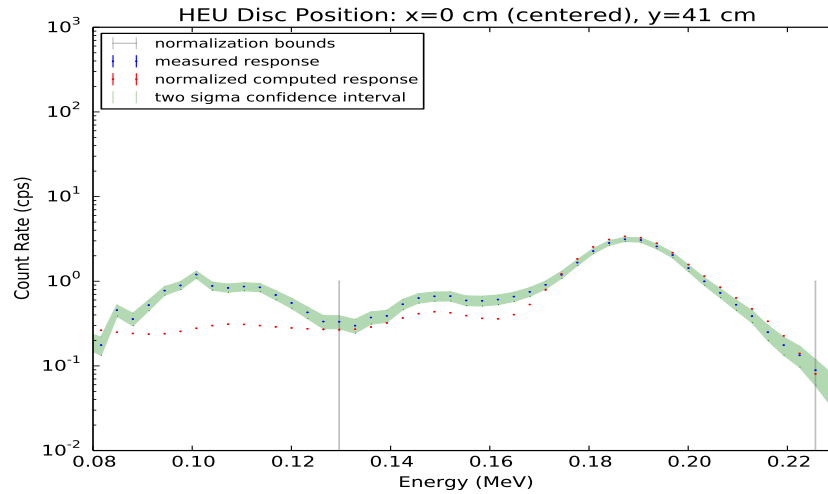
Figure 4.4 Measured and normalized computed responses for the HEU disc at the central position.

The normalized computed spectrum approximated the measured spectrum fairly well (within two standard deviations of the experimental response) for the main full energy peak at 186 keV and its shoulder peak at 205 keV with only a slight overestimation, however the secondary peaks at 163 and 144 keV are underestimated to compensate through normalization. The HEU gamma radiation energies are too low in this case to produce much of a Compton continuum, and any continuum that was produced is obscured by secondary peaks. So, it follows that absorption from the collimator

created a significant decrease in flux unaccounted for by the DRF. The cross sections from Table 4.1 verify this line of thought by demonstrating an absorption cross section that is about 10 times larger than the scattering cross section at 200 keV.

Table 4.1 Various photon cross sections (cm^2/g) from 60 keV to 2 MeV. [25]

Energy (MeV)	Coh. Scattering	Inc. Scattering	Absorp.	Total
6.000E-02	4.900E-01	9.734E-02	4.432E+00	5.020E+00
8.000E-02	3.078E-01	9.923E-02	2.012E+00	2.419E+00
8.800E-02	2.632E-01	9.928E-02	1.547E+00	1.910E+00
8.800E-02	2.632E-01	9.928E-02	7.321E+00	7.684E+00
1.000E-01	2.128E-01	9.894E-02	5.237E+00	5.549E+00
1.500E-01	1.049E-01	9.484E-02	1.815E+00	2.015E+00
2.000E-01	6.260E-02	8.966E-02	8.464E-01	9.986E-01
3.000E-01	2.988E-02	8.036E-02	2.930E-01	4.032E-01
4.000E-01	1.746E-02	7.310E-02	1.417E-01	2.323E-01
5.000E-01	1.143E-02	6.734E-02	8.257E-02	1.613E-01
6.000E-01	8.060E-03	6.263E-02	5.406E-02	1.248E-01
8.000E-01	4.621E-03	5.537E-02	2.871E-02	8.870E-02
1.000E+00	2.991E-03	4.993E-02	1.810E-02	7.102E-02
1.022E+00	2.865E-03	4.944E-02	1.732E-02	6.962E-02
1.250E+00	1.930E-03	4.476E-02	1.168E-02	5.875E-02
1.500E+00	1.347E-03	4.075E-02	8.321E-03	5.222E-02
2.000E+00	7.626E-04	3.482E-02	5.034E-03	4.607E-02

In terms of mean free paths (mfp), the 3 cm of lead provided by the collimator is approximately 29 mfp in terms of absorption and only three mfp in terms of incoherent scattering. The collimator is now optically thick in terms absorption but still thin in terms of scatter. While scattering will still only reduce the flux of the highest full energy peak of the spectrum, it would add to the flux of the lower energy peaks. This explains the overestimation of the high energy peak balanced with the underestimation of the lower peak. The scattering also distorted the shape of the two convolved peaks at 163 and 144 keV really only producing a peak at about 150 keV. Since simulation of the low fidelity results with the peaks combined and averaged in position and intensity yielded better results than the two simulated separately, they were kept together for all subsequent simulations. The comparison of the low fidelity runs with the peaks separated and combined can be found in the Appendix A.1.

The lowest energy peaks below the normalization bounds were originally thought to be a set of

four very low intensity peaks. However, upon further investigation it was found that the backscatter peaks from the three main full energy peaks were of the same energy. Using the Compton scattering equation in terms of energy, it was calculated that the backscatter peaks from the lead shielding would be centered at 114, 108, and 95 keV for the full energy peaks at 205, 186, and 150 keV, respectively. Backscattering that occurs inside the detector crystal is accounted for by the DRF, but that which occurs in the lead shielding is not. Therefore, the backscatter peaks are acknowledged, but excluded from the normalization region in order to avoid skewing the other validation regions.

It is worthy to note that two other factors could have also contributed to the underestimation of the two secondary peaks besides scattering in the collimator. Scattering within the table and aluminum tee that were not simulated in the MCNP fluence model, and gamma rays emitted by the decay products of U-234, U235, and U-238 could also have made some contribution. It was assumed that scattered photons from the table and tee would be negligible due to shielding provided by the collimator. Gamma radiation from uranium daughter products, however, were not simulated simply because there were too many low energy gamma rays with low relative yields (probability of emission per decay).

The HEU disc at the first position: 5 cm off-axis, was counted for a total of five hundred seconds. Measurements were taken in both the positive and negative x directions. The normalized computed and measured responses of both measurements are shown by Figure 4.5.
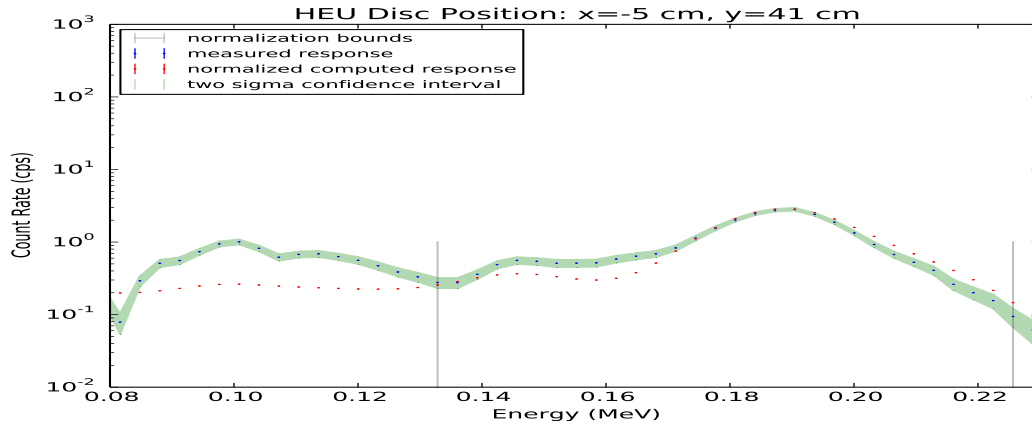
(a)
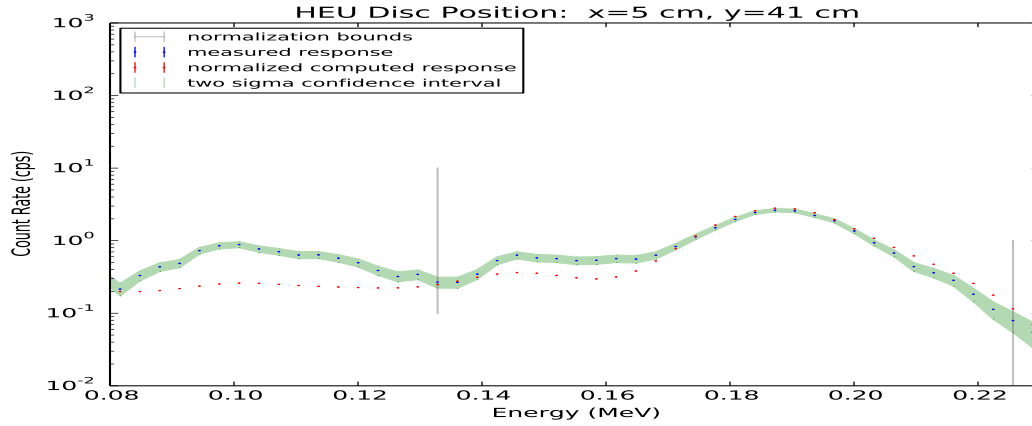
(b)

Figure 4.5 Measured and normalized computed responses for the HEU disc source at y=41 cm and (a) five centimeters left of center x=-5 cm and (b) five centimeters right of center x= 5 cm.

As expected, the entire count rate for both spectra have decreased slightly (about 25%) from the central position due to attenuation with the collimator and increased distance from the source. The lead backscatter peaks have also consolidated into a slightly different shape to accommodate a new more favorable set of scattering angles. The computed response again overestimates the main full energy peak and underestimates the secondary peaks due to the increased scatter from the collimator. Finally, normalization bounds remained the same as the central case.

The second position was 10 cm off-axis, and the HEU disc source was counted for 750 seconds.

The source at the third position (15 cm off-axis) was counted for 1600 seconds. The normalized computed and measured repsonses for the positive and negative axis positions at x=10 cm and x=15 cm are contained in Figure 4.6

(a)

(b)

(c)

(d)
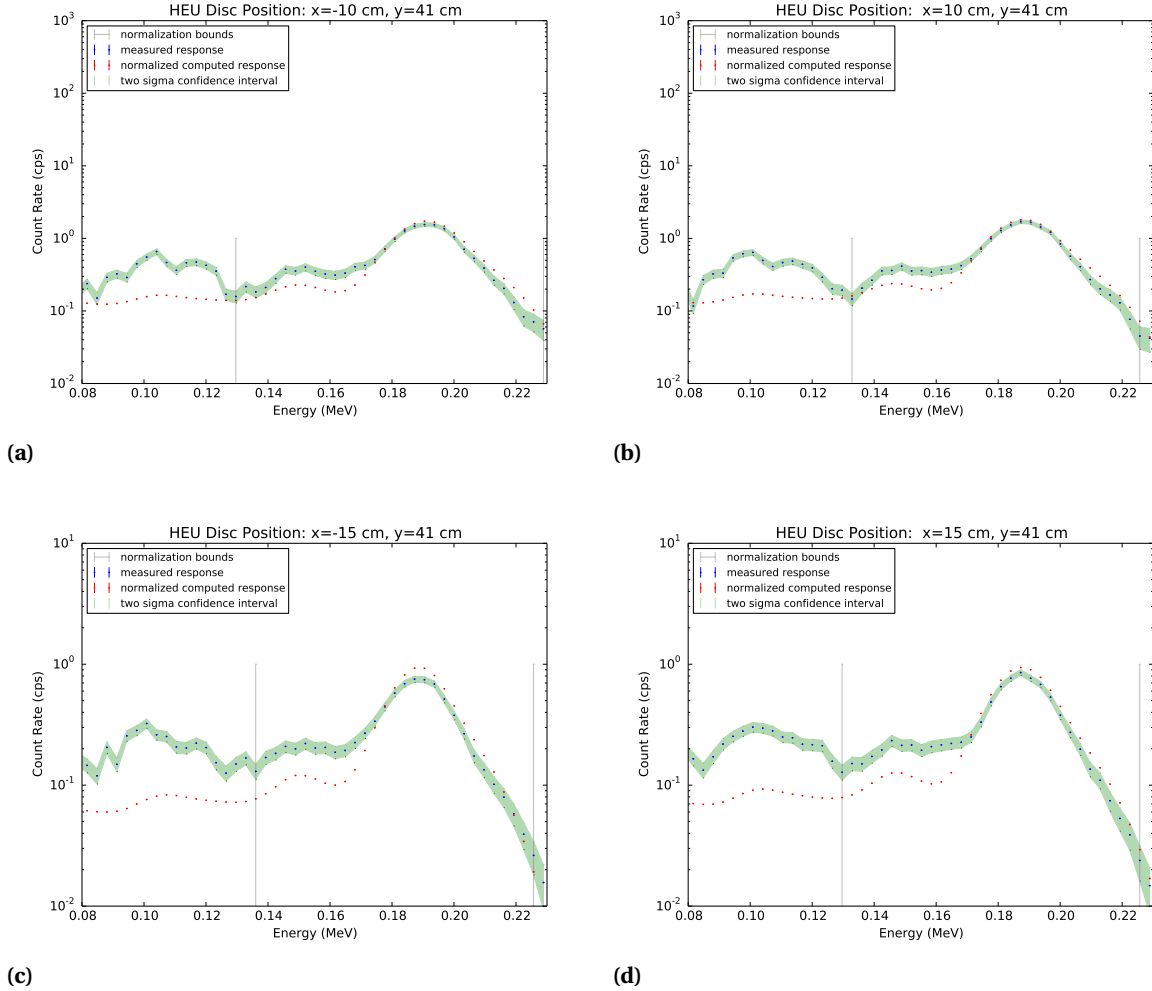
Figure 4.6 Measured and normalized computed responses for the HEU disc source at y=41 cm and (a) ten centimeters left of center x=-10 cm, (b) ten centimeters right of center x=10 cm, (c) fifteen centimeters left of center x=-15 cm, and (d) fifteen centimeters right of center x=15 cm.

The decreasing response trend continues for both positions (10,15 cm) with increased attenuation from the collimator and increased distance. At 15 cm, the secondary peak and the lead

backscatter peaks become nearly indistinguishable from background radiation. The reason for this high background is that the experiment was designed to ensure only the visibility of the main 186 keV peak. Even the least squares fit for the linear shifting process could not fit a Gaussian peak to the 150 keV peak for the x=-15 cm position in Figure 4.8c. So, only a one peak based shift was performed on this spectrum. Normalization bounds remained the same as previous cases for simplicity.

The final position (20 cm off-axis) was most influenced by background and required a long count time in order to overcome it. The HEU disc at 20 cm was counted for 4800 seconds. The normalized computed and measured responses are shown by Figure 4.7.
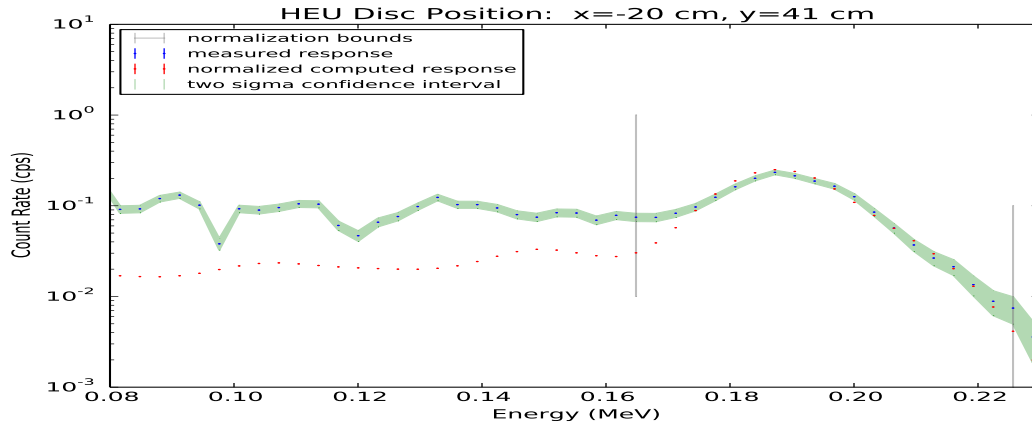
(a)
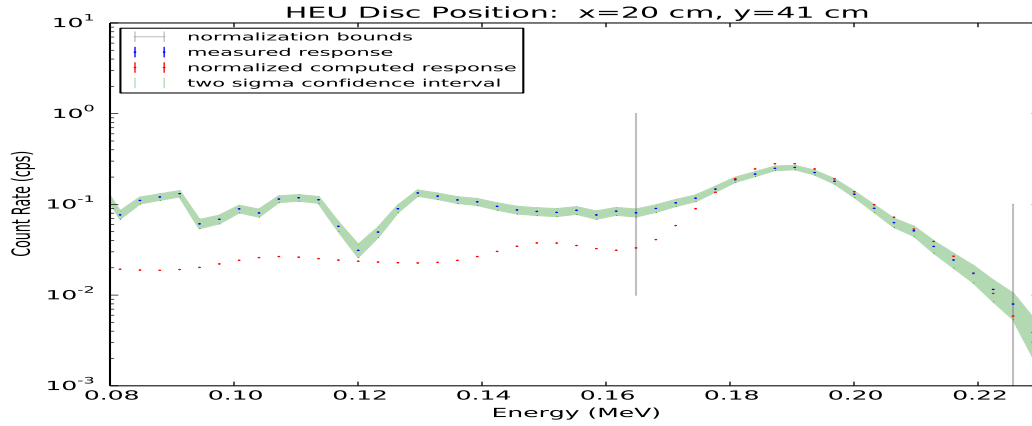
(b)

Figure 4.7 Measured and normalized computed responses for the HEU disc source at y=41 cm and (a) twenty centimeters left of center x=-20 cm and (b) twenty centimeters right of center x= 20 cm.

The count rate for this position was the lowest and most attenuated. Again, in order to focus on the main peak and maintain reasonable count times, only the main peak at 186 keV was resolved from background. Furthermore, the normalization was narrowed to only contain the main peak range. The normalized simulated response approximates peak behavior quite easily in spite of collimation and geometry when isolated from the rest of the spectrum.

4.4   HEU Disc Attenuation Measurement Set

The second set of HEU disc measurements were done in the interest of testing the DRF model's simulation of purely attenuated responses. Each measurement was performed centered on-axis at a distance of 11 cm from the crystal (only 8 cm from the face). The first measurement was counted without any attenuators. The second and third cases involved taping one and two stainless steel plates, respectively, to the face of the detector. The count time was kept constant at 300 s for all three measurements. The normalized computed and measured responses for all three cases are contained in Figure 4.8

(a)

(b)

(c)
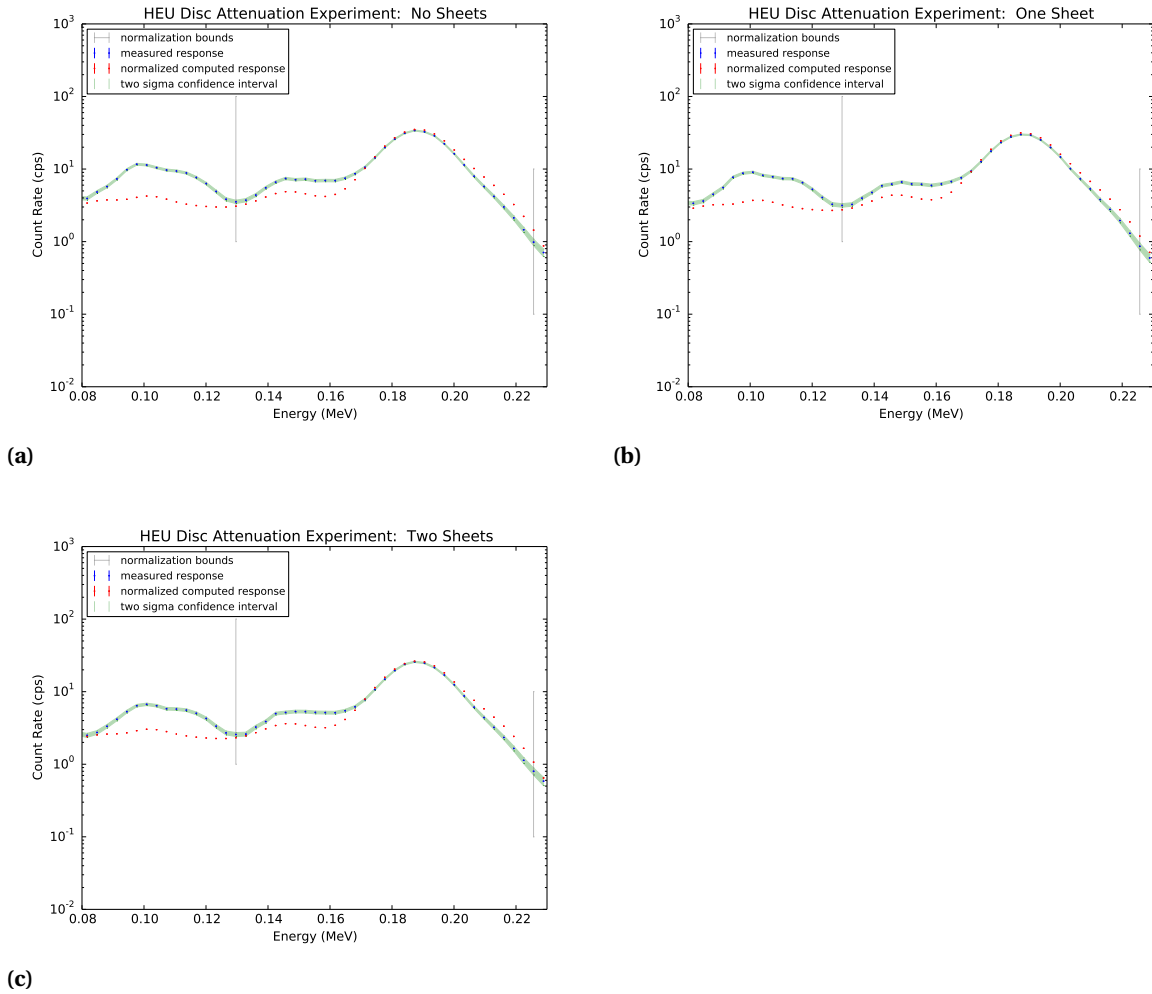
Figure 4.8 Measured and normalized computed responses for the HEU disc source with (a) no, (b) one, and (c) two stainless steel sheets taped to the detector face.

The same effects as observed before for the central position at 41 cm is observed for the unattenuated response: imbalance between the two full energy peaks and no prediction of the lead backscatter peak. However, the count rate is higher due to the closer proximity of the source. Naturally, the normalization bounds were kept the same as the inner axial HEU measurements. As stainless steel sheets are added to the face of the detector, a decrease in count rate across the entire spectrum is observed. The effect is very similar to that of the off-axis cases, except the background shape does not change since the angle of incident radiation is constant.

CHAPTER

5

UNCERTAINTY QUANTIFICATION

The other major goal is to quantify the uncertainties associated with the simulated responses that were used to validate the 1x2" NaI ORNL field detector. Validation reveals the accuracy of the model whereas uncertainty yields the expected precision of the simulated responses providing a level of confidence in the results. Each step in calculating the detector responses for each case has an associated uncertainty that has been calculated and compared to the experimental uncertainty where applicable.

Uncertainties that were easily reducible (e.g. MCNP uncertainties are based on the number of histories run), were always reduced below the peak channel uncertainty for each measurement case. Fitting uncertainties were based on the number of data points and the data uncertainty and therefore constrained to the quality of measurements performed. Even so, most of the fixed uncertainties tended to be under the respective measurement's experimental uncertainty.

5.1   Monte Carlo Based Uncertainties

The first quantity required to calculate a simulated response is the MCNP fluence calculated by particle track length tallies in MCNP. The fluence tally was divided into small energy bins according to the energy structure of the DRF calculated by g03. MCNP calculates the relative uncertainty of

each bin based on the number of particle track lengths that fall into that bin. Therefore, the number of total tallies were chosen in order to make the energy bin with the highest standard deviation have the same uncertainty as the lowest experimental uncertainty for each measurement excluding the Am-241 seed peak region. The number of histories required was then easily predicted, since again Monte Carlo standard deviation is equal to the inverse square root of the number of particle histories. In all cases, excluding Co-60, the number of histories required was on the order of billions. Similarly, in the Cs-137, Co-60, and HEU attenuation cases the highest computational uncertainties above 80 keV were ensured to be below the lowest uncertainty of the experimental results.

In certain cases of the HEU disc measurements at forty one centimeters, meeting the lowest experimental uncertainty for every tally energy bin was difficult to do in a reasonable amount of computational time. Certain MCNP modeling measures were taken to compensate and reduce computation times. First, the lowest energy bins below 80 keV were excluded for two reasons. These bins had the highest computational uncertainty, and they were overshadowed by leftover noise from the background subtraction of the Am-241 seed peak in the measured spectrum anyway.

The other change involved simply reducing the source definition from an isotropic source to only producing particle histories within the solid angle calculated to actually strike the detector whole, not just the face. All particles were then weighted using a form of importance sampling called forcing to prevent biasing the fluence tally, where the alternate pdf was uniform over the reduced angle and the original pdf was uniform in all directions. The modified pdf ($\tilde{f}(x)$) and the weighting factor (w) can be derived from Equations 5.1 and 5.2 respectively.

$$\tilde{f}(x) = \frac{f(x)}{\int_{x_1}^{x_2} f(x)dx} \; for \; x_{min} \leq x_1 \leq x \leq x_2 \leq x_{max}, \tag{5.1}$$

$$w = w_0 \frac{\int_{x_1}^{x_2} f(x)dx}{\int_{x_{min}}^{x_{max}} f(x)dx}, \tag{5.2}$$

where w is the forced weight of the particle and w_0 is the original weight of the particle. $f(x)$ is the original pdf, and x_1 and x_2 are the new bounds to be imposed on the pdf in order to only sample the important region contained by them. [26] In our work, the initial source distribution direction was modified from being isotropic in all directions to being contained within the angle cosine relative to a directional vector ($\vec{v}$) aligned with the center of the detector face but still isotropic in the other directions. A diagram of the detector to source geometry is shown for reference in Figure 5.1.
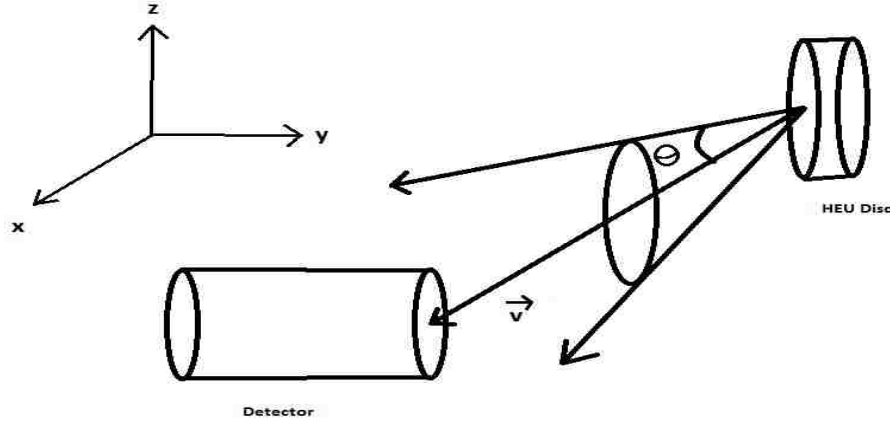
Figure 5.1 Diagram of the detector to source geometry and the solid angle chosen for the initial source distribution forcing pdf.

If μ_c is the cosine of angle θ (chosen to include the whole detector surface area), and the original pdf is $f(x) = d\mu/2$. The solid angle bounds are set to $x_1 = \mu_c$ and $x_2 = 1$ for a narrower forward direction. The modified pdf becomes

$$\tilde{f}(\mu) = \frac{\frac{d\mu}{2}}{\int_{\mu_c}^{1} \frac{d\mu}{2}} = \frac{d\mu}{1-\mu_c}, \tag{5.3}$$

which is sampled from instead of the full isotropic pdf. The corresponding weight can be derived as

$$w = w_0 \frac{\int_{\mu_c}^{1} \frac{d\mu}{2}}{\int_{-1}^{1} \frac{d\mu}{2}} = w_0 \frac{1-\mu_c}{2}, \tag{5.4}$$

which is multiplied by the original weight of each particle emitted from the source. This change reduced the variance significantly allowing a more reasonable amount of particles to be run for the $x = \pm 15$ cm and $x = \pm 20$ cm cases.

Since the table and room geometry are not simulated in the MCNP model anyway, it is a small approximation assuming that off direction photons would likely escape the system of interest.

Rather than show all of the bin uncertainties for each case, the case with the highest uncertainty (HEU disc at x=41 cm, y=-20 cm) excluding the Co-60 measurement will be given as an example. The fluence F4 tally is plotted with its uncertainty bounds in Figure 5.2.
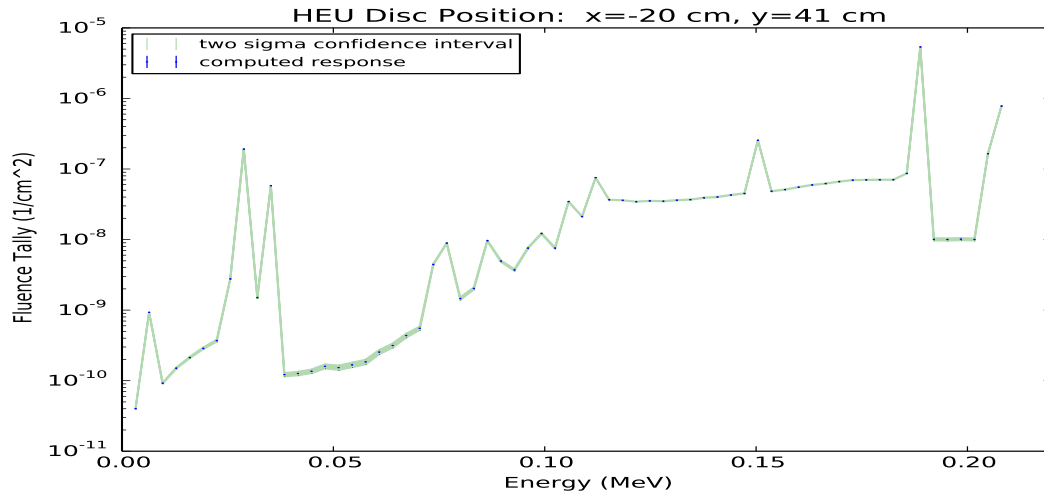
Figure 5.2 MCNP computed fluence and two sigma confidence interval

The bounds are fairly narrow beyond 80 keV. Each spike in the fluence corresponds to an incident gamma ray energy from the HEU disc starting from 105 keV and ending at 205 keV. The highest relative standard deviation greater than 80 keV was 2.44% at 195 keV. This was well below the lowest relative standard deviation of the HEU disc measurements at 41 cm which was 2.72%. As can be seen, the confidence bound between the 186 keV peak and the maximum energy peak at 205 keV is wider than anywhere else above 80 keV. Even the bins in under 80 keV did not exceed 5% relative standard deviations.

The DRF itself contains a Monte Carlo calculation that fully calculates the probabilities of a count in each channel based on contributions from all other channels using the fit parameters. Once again, the number of particle histories controls the relative uncertainty of the DRF, and the same threshold of the lowest experimental uncertainty for each case was selected for the highest DRF channel uncertainty. The order of particles required was much less than that of the flux calculations and only on the order of hundreds of thousands for all DRF Monte Carlo calculations.

Again, it is not feasible to show every uncertainty for each measurement, so only the highest uncertainty case (excluding Co-60) will be shown. As expected, this case would be the HEU disc at forty one centimeters for the off-axis experiments. Furthermore, six DRFs (one for each incident photon energy) are summed together to produce the total DRF, so the peak DRF with the highest uncertainty was chosen (105 keV peak). Because g03 did not have a second axis distance variable, only one total DRF was used for the off-axis HEU disc experiments. Now, since the full DRF depends

on two variables and would produce a three dimensional surface plot it will be easier to display the uncertainty bounded along the peak channel densities, as displayed in Figure 5.3.
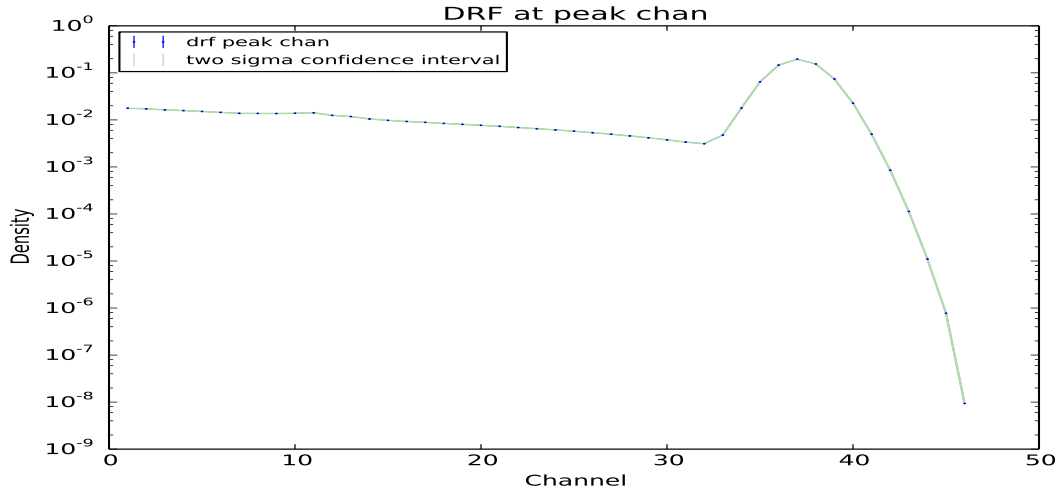
Figure 5.3 HEU disc at 41 cm with DRF densities for the 105 keV peak at channel 33 and the two sigma confidence interval

The highest probability density channel contributions for channel 33 are the immediate channels above that channel as expected from the spread of Gaussian uncertainty. However, the peak of the densities is actually about five to six channels over channel 33 which might explain the need to shift the computed spectra about the same number of channels. Channels above the spread have no contribution (density=zero), and the channels below are fairly constant. When the entire DRF is multiplied by the flux, the entire row of densities for each channel is multiplied by the flux vector and summed, so naturally the uncertainty is constant for each channel. The relative standard deviation for this channel was 0.420% and well under the 2.72% experimental uncertainty. Each channel row in the DRF possesses a similar density curve, so the highest flux channel will produce the highest response automatically. The highest relative standard deviation of all the DRF channels was for the last channel (512) and was only 1.80%.

The total absolute efficiency calculation was carried out through calculation with an XCOM NaI cross section and particle track lengths through the crystal volume in MCNP as described by Equation 3.5. The number of histories were increased accordingly until the proper number of path lengths were acquired to reduce the highest relative standard deviation to approximately that of

the lowest experimental uncertainties. The highest uncertainty case is shown for the HEU disc at forty one centimeters. The resulting density curve with a two sigma confidence interval is shown in Figure 5.4.
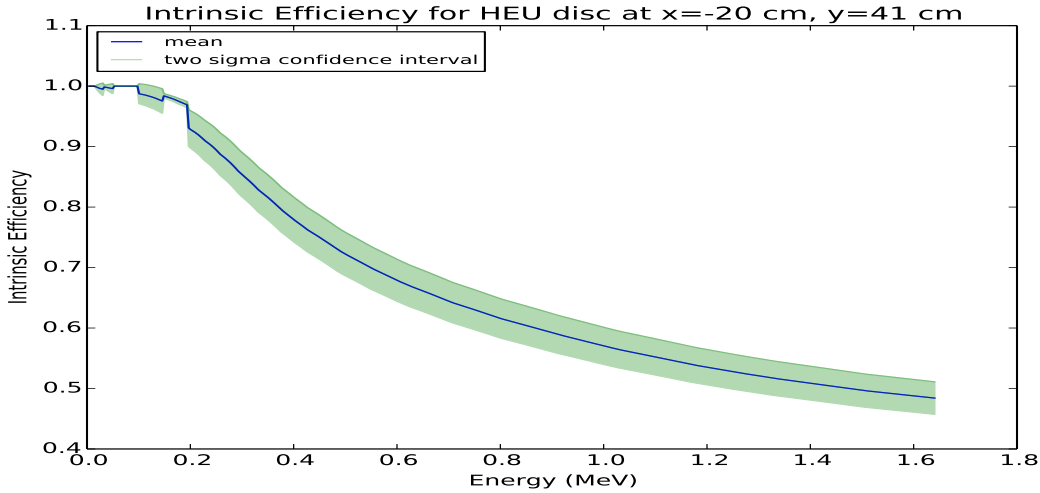
Figure 5.4 Absolute efficiency of the HEU disc at 41 and two standard deviation confidence interval

This curve is essentially the probability of an interaction of energy E, occurring within the crystal. So, low energies are almost certain to be absorbed and higher energies are more likely to escape. The relative uncertainty is fairly small at low energies, but grows as energy increases. The relative standard deviation was 2.78% at the highest energy which was close to the lowest experimental relative uncertainty of 2.72%. At 0.2 MeV or less where the majority of the HEU spectrum lies the relative uncertainty is much lower and well below 1%. The higher uncertainty at higher energies is purely a factor of lack of information or no particle tracks at those energies.

5.2 Parameter Uncertainties

The first set of parameters are associated with both the measured and computed results: the energy calibration. The energy calibration is simply a polynomial that converts channel data to energy data based off of the nonlinear scintillation behavior of NaI detectors. This is a necessary piece for verifying physical measurements and a required conversion for the empirical power law of the DRF. The energy polynomial is given by Equation 5.5

$$E(keV) = \alpha_2 x^2 + \alpha_1 x + \alpha_0, \tag{5.5}$$

where x is the channel, E is energy in keV, and α_0, α_1, and α_2 are the polynomial parameters. The energy calibration parameters were found by a least squares fit of measurements of known sources with known energies at the gain settings discussed in Section 3.1. Three sources were used to determine the energy calibration polynomial: the Am-241 seed source, and the Cs-137 and Co-60 sources detailed in Table 3.1. Each channel mean for the energy calibration was found by taking the peak section of the measured responses for each source and fitting them according to a simple Gaussian plus linear background empirical model. The linear Gaussian model is given by Equation 5.6

$$G_y = \frac{B}{\sqrt{2\pi}\sigma_T} e^{-\frac{1}{2}(\frac{x-\bar{x}}{\sigma_T})^2} + a_1(x-\bar{x}) + a_0. \tag{5.6}$$

where x is the detector channel and G_y is the resulting point in the Gaussian curve. B is the normalization constant, and σ is the standard deviation of the Gaussian. Finally, $\bar{x}$ is the mean of the Gaussian, and a_0 and a_1 form the linear background term. The Gaussian channel means and parameter standard deviations are shown in Table 5.1.

Table 5.1 Channel means and associated standard deviations (STD) of the Gaussian fits for the energy calibration.

Source	Pk. No.	Mean Chan., $\bar{x}$	STD, $\sigma^{\bar{x}}$	Rel. STD, $\sigma^{\bar{x}}_{rel}$ (%)	Red. Chi-Square, χ^2_ν
Am-241	1	20.92	2.767E-3	1.323E-2	0.8973
Cs-137	1	195.79	1.804E-2	9.212E-3	2.569
Co-60	1	341.64	0.2214	6.479E-2	1.059
Co-60	2	386.38	0.1761	4.557E-2	0.7260

Each least squares fit was performed by a nonlinear least squares algorithm in MATLAB called lsqnonlin. The standard deviation was found through the simple Frequentist methods described in Section 2.5 from the parameter covariance matrix. Classical Frequentist methods were used in lieu of Bayesian for all Gaussian peak fitting except for the power law measurements because there were usually a larger number of points in each peak. Also, Frequentist calculations require less calculation time than DRAM (about 100 times less). The algorithm had no trouble fitting these peaks, as each relative standard deviation of the mean channel is well under 1%. Co-60, as expected, had the highest uncertainty because it had the lowest source strength and a low count time (low

fidelity measurement). However, all peaks were well approximated by the model producing reduced chi-squares well under ten.

A similar least squares fit was performed by lsqnonlin using the energy polynomial (Equation 5.5). The resulting parameter means and standard deviations are tabulated in Table 5.2.

Table 5.2 Energy calibration parameter means and standard deviations.

Parameter	Mean	STD., σ	Rel. STD, σ_{rel} (%)	χ_ν^2
a_2	2.104E-4	4.352E-5	20.68	530.4
a_1	3.395	1.762E-2	0.5188	
a_0	-11.07	1.382	12.48	

Since there were a low number of data points for the energy calibration fit, the Bayesian code DRAM was used to calculate the standard deviations and optimize the parameter means from the least squares starting values. NaI is fairly linear in terms of scintillation to energy deposited ratio for low energies, so it is no surprise that the second order term is very small. Unfortunately, this also means that it has a larger relative standard deviation. The y-intercept term (a_0) has a little more effect but also has more uncertainty than the first order term (which holds the lowest uncertainty at about half of a percent).

In order to check DRAM for a possible error in the fit and uncertainty calculations, a standard linear regression fit with Frequentist calculations was calculated for comparison. A slightly better reduced chi-squared value of 430.5 was found, and the parameter values were modulated within 1% of the Bayesian values. The uncertainties were also halved. So, in this case, it may actually have been slightly better to use the standard linear regression, however, the improvement in the results would have been marginal.

Overall, the calibration still performed well in spite of the poor reduced chi-squared value, as each channel mean converted to energy was found to be within two keV (1% relative error) from its true value for all peaks that were not convolved with another peak (e.g. the 150 keV convolved HEU peak). This is acceptable because the same energy calibration is used for both computed spectra and measured spectra. So, any additional error would offset both spectra by the same amount.

The next set of parameters involves the power law of the DRF model itself. g03 not only uses Monte Carlo simulation to calculate DRFs, but requires an empirically fit power law based on Gaussian spread data from the detector of interest. The power law is the very same described in the DRF model section of the Literature review by Equation 2.3.

Again, linear Gaussian (Equation 5.6) least squares fits of several sources were required to obtain mean Gaussian standard deviations for the power law. Five sources were used: Am-241 (seed source), Ba-133, Cs-137 (same as in Table 3.1), Mn-54, and Na-22. Since Ba-133 has two full energy peaks, a total of six full energy peaks were fit.

Source geometry and activity were not required for the power law fit. However, each peak was counted until 10,000 counts were registered in the peak channel to keep the experimental uncertainty close to one percent in the peak region. Some weak sources needed multiple measurements added together to meet 10,000 counts due to the MCA timer limit. Furthermore, there should be no added uncertainty in the measurements because the spectra were checked for gain drift and perfomred immediately after one another. The mean Gaussian standard deviations ($\sigma_T(E_I)$) and their uncertainties are compiled in Table 5.3.

Table 5.3 Channel means and associated standard deviations of the Gaussian fits for the power law.

Source	Pk. No.	Energy (MeV)	Gauss. STD, σ_T	STD, σ^{σ_T}	Rel. STD, $\sigma_{rel}^{\sigma_T}$ (%)	χ_ν^2
Am-241	1	5.954E-2	4.454E-3	2.128E-5	0.4778	0.9191
Ba-133	1	8.100E-2	4.879E-3	4.478E-4	9.177	56.51
Ba-133	2	3.560E-1	1.499E-2	2.106E-4	1.405	13.09
Cs-137	1	6.617E-1	2.137E-2	7.599E-5	0.3556	2.295
Mn-54	1	8.348E-1	2.468E-2	8.469E-5	0.3432	1.011
Na-22	1	1.275	3.207E-2	8.001E-5	0.2495	1.611

Some of the peaks involved in the Gaussian fits for the power law spread data were sparse in data points, so DRAM was used to optimize the Gaussian spread parameter means (σ_T) and determine their respective standard deviations (σ^{σ_T}). The first Ba-133 peak suffered quite a bit of background interference from convolution with the Am-241 peak, and had fewer points to fit the linear Gaussian curve to resulting in the highest uncertainty and a reduced chi-square well over ten ($\chi_{red}^2 \leq 10$ is considered a good fit). The first peak's data was almost thrown out for its poor Gaussian fit. The second Ba-133 peak was also over 1% in relative uncertainty and had a reduced chi-square over ten (to a much lesser extent than the first). This was probably due to some interference with a third lower intensity peak at 300 keV obscuring the left tail of the Gaussian.

As a follow up, examining the linear correlation coefficients of a model can reveal weak model parameters. If the correlation coefficients of a parameter are all under about 0.2, then that parameter shares no linear relationship to any of the other parameters. Sometimes, removing such parameters from the model can improve the fit. An example of this model will be provided using the worst fit

case to check for model weaknesses. The linear correlation coefficient matrix for the first Ba-133 peak (81 keV) is listed as Table 5.4.

Table 5.4 Linear correlation coefficients for the 81 keV Ba-133 linear Gaussian model fit.

Parameter	σ_T	$\bar{x}$	B	a_0	a_1
σ_T	1	-0.9594	0.9901	-0.9838	0.9737
$\bar{x}$	-0.9594	1	-0.9727	0.9664	-0.9801
B	0.9901	-0.9727	1	-0.9978	0.9922
a_0	-0.9838	0.9664	-0.9978	1	-0.9936
a_1	0.9737	-0.9801	0.9922	-0.9936	1

All of the coefficients are very highly correlated (>0.9), so there are no weak parameters. This does not mean that the model cannot be improved, just no terms should be removed. Maybe a few terms could be added to account for the nonlinear tail of the 60 keV Am-241 seed peak, however, a more practical alternative was found by weighting the power law fit by the x-data uncertainties at each point.

This alternative was developed in response to the higher uncertainty in the Ba-133 peaks and the distrust in the Am-241 seed peak due to lack of exact knowledge of the seed's position relative to the center of the crystal. Originally, only three sources were used to calibrate the DRF power law, but results showed some error in the peak widths of some of the validation measurements. To counter this issue, the power law fit was thought to be improved with extra measurements at energies between the three original points. However, rather than throw out less than ideal data points for the power law, the least squares fit was simply adjusted to weight each data point by its uncertainty. Instead of purely minimizing the sum of squares (classical least squares), the weighted sum of squares (Equation 5.7) was minimized.

$$WSS_q = \sum_{i=1}^{n} \left(\frac{\Upsilon_i - f(x_i, p_j)}{\sigma(x_i)}\right)^2 \tag{5.7}$$

Above, n is the total number of data points. Υ_i is the measured result at data point i, and $f(x_i, p_j)$ is the value of the function being fit to the data at i. p_j are the parameters, and $\sigma(x_i)$ is the standard deviation of Υ_i used as a weight. In this case the function fit was the power law, Equation 2.3, and Υ was simply $\sigma_T(E)$.

The rest of the least squares and uncertainty calculations remained the same. The resulting parameter means and standard deviations of the weighted power law fit are in Table 5.5.

Table 5.5 Power law parameter means and standard deviations.

Parameter	Mean	Standard Deviation, σ	Relative STD, σ_{rel} (%)	χ^2_v
a	0.027608	1.684E-4	0.6100	8.500E-6
b	0.644237	5.719E-3	0.8877	

There were several data points for the power law, and it was uncertain if the weighted sum of squares would behave well with the Bayesian code. So, the classical Frequentist values were used in the DRF calculations for expedience. The Bayesian code was tested later and gave comparable results which are given in Appendix A.2. The parameter values are on the order of Peplow and Heath's power law coefficients, and the relative standard deviations are under 1%. The power law is a bit overfit, but that is somewhat expected as several extra measurements were taken when the three point fit proved insufficient.

The final process requiring uncertainty quantification is the linear energy shift required to align the computed and measured spectra. g03 contains a small bug that tends to offset the entire spectrum by several channels to the right. A program called gshift (courtesy of Gardner's group) corrects this issue by linearly interpolating between the channels and shifting the pulse height spectrum to the desired channels according to Equation 5.8

$$x_{chan} = A \cdot E_p + B, \tag{5.8}$$

$$E_p = E \cdot f(E),$$

where x_{chan} is the channel number, and A is a normalization constant. B is the number of background channels, and E_p is the energy of the original pulse-height spectrum. Finally, E is the true energy of the gamma-ray (or desired energy to shift the peak to), and f(E) is the functional relationship of the ratio: Ep/E. A and B are adjusted accordingly to shift the peak(s) to the desired location, while f(E) is chosen by the user. Either f(E) is based off of the natural NaI nonlinearity (for two or more peaks), or directly proportional (for one peak).

In order to determine the linear shift required, the mean peak channels of both the measured and computed spectra had to be found. The means were found in the same manner as those for the energy calibration fit, by fitting the spectral peaks to the linear Gaussian model (Equation 5.6). The Gaussian peak channel means and the associated uncertainties for the computed spectra are given by Table 5.6 and those of the measured spectra by Table 5.7.

Table 5.6 Computed spectrum channel means and associated standard deviations of the Gaussian fits for the energy energy shift.

Source	Pk. No.	Mean Chan., $\bar{x}$	Stand. Dev., $\sigma^{\bar{x}}$	Rel. STD, $\sigma^{\bar{x}}_{rel}$ (%)	χ^2_ν
Cs-137	1	204.67	9.799E-3	4.788E-3	1.528E-4
Co-60	1	354.68	1.310E-2	3.692E-3	3.867E-6
Co-60	2	397.71	7.363E-3	1.851E-3	1.985E-6
HEU Rad.					
Center	1	52.22	1.610E-2	3.084E-2	3.257E-3
Center	2	64.51	1.093E-2	1.695E-2	0.2371
L1	1	52.22	1.596E-2	3.056E-2	1.586E-3
L1	2	64.51	1.072E-2	1.661E-2	0.1116
L2	1	52.23	1.527E-2	2.924E-2	4.388E-4
L2	2	64.51	1.069E-2	1.656E-2	3.294E-2
L3	1	52.24	1.442E-2	2.760E-2	1.318E-4
L3	2	64.51	1.090E-2	1.689E-2	1.127E-2
L4	1	52.26	1.272E-2	2.433E-2	3.262E-5
L4	2	64.52	1.174E-2	1.819E-2	4.119E-3
R1	1	52.22	1.592E-2	3.049E-2	1.576E-3
R1	2	64.51	1.073E-2	1.663E-2	0.1122
R2	1	52.23	1.523E-2	2.916E-2	4.344E-4
R2	2	64.52	1.073E-2	1.663E-2	3.309E-2
R3	1	52.24	1.450E-2	2.775E-2	1.318E-4
R3	2	64.52	1.095E-2	1.698E-2	1.141E-2
R4	1	52.25	1.282E-2	2.453E-2	3.303E-5
R4	2	64.52	1.156E-2	1.791E-2	3.971E-3
HEU atten.					
0 sheets	1	52.15	2.380E-2	4.564E-2	2.151E-2
0 sheets	2	64.46	3.873E-3	6.008E-3	7.474E-2
1 sheet	1	52.13	2.600E-2	4.987E-2	2.249E-2
1 sheet	2	64.45	3.312E-3	5.139E-3	4.582E-2
2 sheets	1	52.12	2.818E-2	5.407E-2	2.286E-2
2 sheets	2	64.44	2.891E-3	4.487E-3	2.658E-2

Table 5.7 Experimental net spectrum channel means and associated standard deviations of the Gaussian fits for the energy shift.

Source	Pk. No.	Mean Chan., $\bar{x}$	Stand. Dev., $\sigma^{\bar{x}}$	Rel. STD, $\sigma^{\bar{x}}_{rel}$ (%)	χ^2_ν
Cs-137	1	195.79	1.804E-2	9.212E-3	2.569
Co-60	1	341.64	0.2214	6.479E-2	1.059
Co-60	2	386.38	0.1761	4.557E-2	0.7260
HEU Rad.					
Center	1	46.90	0.8512	1.815	0.5671
Center	2	58.30	3.464E-2	5.942E-2	8.139E-2
L1	1	45.84	0.1005	0.2192	6.329E-2
L1	2	58.54	0.1584	0.2706	0.9686
L2	1	46.2	0.4500	0.9740	1.626
L2	2	58.55	0.2289	0.3910	1.060
L3	1	X	X	X	X
L3	2	58.51	0.1789	0.3057	0.8369
L4	1	X	X	X	X
L4	2	58.23	0.1407	0.2416	1.837
R1	1	45.94	0.1990	0.4332	0.8888
R1	2	58.34	0.1473	0.2525	1.168
R2	1	46.02	0.3772	0.8197	0.8361
R2	2	58.35	0.1200	0.2057	0.5307
R3	1	46.25	0.4760	1.029	0.9318
R3	2	58.20	0.2007	0.3449	2.701
R4	1	X	X	X	X
R4	2	58.54	0.2326	0.3973	1.716
HEU atten.					
0 sheets	1	46.02	0.2425	0.5269	3.488
0 sheets	2	58.37	6.708E-2	0.1149	1.298
1 sheet	1	46.12	0.3239	0.7023	4.015
1 sheet	2	58.32	7.000E-2	0.1200	1.248
2 sheets	1	45.99	0.3881	0.8438	5.661
2 sheets	2	58.33	5.568E-2	9.545E-2	1.104

    All of the computational channel relative standard deviations were well under 1% (lowest Poisson uncertainty estimated from highest peak channels), but not all of the net (background subtracted) experimental ones were. However, the experimental channel uncertainties that were over 1% occurred only in the lower intensity 150 keV peak of forty one centimeter HEU disc measurements. Furthermore, those uncertainties were expected to be higher as the lowest peak channel poisson uncertainty of the forty one centimeter HEU measurements was 2.72%. Some of the reduced chi-

square values showed some overfitting (perhaps the linear background was unnecessary for the computed results), but none of the values were over ten.

All of the computational peak fits naturally had much lower uncertainties then the experimental peak fits. Some of the 150 keV experimental peaks of the far off-axis HEU disc measurements were not well developed, and could not be fit. In these cases, the shifting program employed the single peak shift algorithm (Equation reference if available here) instead using only the main 186 keV peak channel means to shift the computed spectrum in alignment with the measured.

CHAPTER

6

CONCLUSION AND FUTURE WORK

The goal of this work was to validate and quantify the uncertainty of Gardner's DRF model for several source types and geometric configurations of a 1x2" NaI detector. How these goals were met has already been detailed in the body of this thesis, but the implications of the results of this work and extensions to future work will be discussed in this section.

6.1 Conclusion

Validation of calibration sources The model aligned within two standard deviations of the measured spectrum of the full energy peaks of the Co-60 and Cs-137 button source spectra, but significantly overestimated the Compton continuum by about 45-60%. At first this discrepancy was thought to be simply an effect of the collimator being unaccounted for by the DRF model, but this hypothesis proved to be incorrect. More light was shed on the discrepancy when a peak normalization of the spectrum instead of the sectional normalization was performed in order to compare spectra with a previous one from Gardner's validation work.

Under peak normalization, the computed spectrum nearly matched with the peak of the measured response, but overestimated the rest of the spectrum. This effect was very similar to one of Gardner's spectra in which the electron range multiplier (Equation 2.4) was set too low. The electron

range multiplier is a semi-empirical model of the electron range that was fit by trial and error. Further details of the fit were not given.

Validation of HEU disc   The HEU validation campaigns consisted of two sets of experiments: one concerning x-axis off-sets of the source from the origin at a y-axis distance of 41 cm, and another one involving attenuation using steel plates for the disc centered on the x-axis at a distance of 11 cm. Both campaigns showed predictable physics effects in terms of backscatter peak distortion and attenuation for each type of geometrical configuration change, but a markedly different effect occurred instead of the continuum overestimation witnessed in the calibration source validation.

Since the full energy peak of U-235 is too low for any sizable Compton scatter losses from the detector crystal, there is no visible Compton continuum in the HEU spectra. Without a continuum, there are only four main peaks observed in the measured spectrum: the main full energy peak (186 keV), the shoulder peak (205 keV), the convolved peak (150 keV), and a few backscatter peaks (around 100 keV). The model reproduced the main peak and its shoulder peak well, again within two standard deviations of the measured count rate, but underestimated the convolved peak and did not reproduce the backscatter peak. The backscatter peak is an artifact of the lead collimator around the detector. This collimator is not accounted for by the DRF model because the model currently only reproduces the effects of scattering within the detector crystal. It is also possible that not accounting for the local geometry of the table and aluminum tee and the daughter product decay photons of the uranium may also have contributed to the secondary peak underestimation.

Uncertainty quantification   Finally, uncertainty quantification of the model was conducted on every calculated quantity from the flux calculation by MCNP to the Gaussian peak fits for the spectral shifting program. Where the uncertainty was controllable by the number of particle histories chosen in Monte Carlo simulations, it was reduced below the lowest measured uncertainty. Where it was constrained to the accuracy of the model for least squares fitting, it was compared to the experimental uncertainty and the reduced chi-square test was performed to check for goodness of fit.

Only two poor fits were observed, out of a total of sixty examined in this work, (in terms of parameter variance and chi-square): the energy calibration and the Ba-133 Gaussian peak fits used for the power law fit. The first was compared with other data points to verify a working accuracy, since the measurement of further known sources was impractical. The largest error between the calculated energy of a peak and its known value was approximately one percent for any non-convolved full energy peak. Because the energy calibration is applied to both the measured and computed spectrum (not affecting any differences between the spectra), it was deemed acceptable.

The poor Ba-133 peak fits were largely caused by the peak convolutions with other peaks. The fit was necessary to obtain the peak standard deviation for the power law fit. Rather than discard

the Ba-133 points, the problem was resolved by weighting the power law fit by the uncertainty in the Gaussian peak width data points using a weighted least squares technique (Equation 5.7). All other parameter uncertainties fell well under the lowest experimental uncertainty and passed the chi-square test, hence they are considered reliable for use in future work.

6.2 Future Work

There are many parameters that could affect the shape of the normalized computed responses produced by the DRF. In order to narrow down the parameters that contribute most to the secondary peaks and the Compton continuum of the spectrum, a parameterization study could be performed. Parameters such as the electron range multiplier, collimator thickness and density, source position and peak intensity, and input cross-sections would be incrementally changed to test the resulting sensitivity of the normalized computed response. The most sensitive parameters could then be prioritized for further study.

The electron range multiplier   This factor was originally said to have been fit by trial and error. Details of experimental data used and how it was fit have not yet been found. Further investigation could be helpful for tuning the factor for new detector configurations. However, it is possible that the parameters were not fit but guessed until a favorable result was found. If so, then it is clear that future experiments should be performed not only to determine the electron range of the 1x2" detector in order to better fit this equation in the g03 source code, but to verify the original parameter choices for Gardner's detectors. A better fit could potentially correct the continuum overestimation problem observed in the calibration validation work reported in this thesis.

Outside detector crystal scattering   g03 could eventually be modified to account for outside detector crystal scattering. Doing so would be highly valuable for a variety of reasons. For one thing, it might allow distinguishing of detector geometry from attenuation by the distortion versus decreased amplitude of the backscatter peak. Being able to do this would be very helpful in inverse problems focusing on unknown radiation source characterization. Some members of Gardner's research group are already addressing this problem.

Verify Assumptions   Several assumptions were made throughout this work, such as modeling the detector PMT and the electronic housing as void, only modeling the photons emitted directly by U-235, and not using the table and aluminum tee in the MCNP model. Further work could be done to check the validity of these assumptions. For example, the detector PMT could be modeled as a homogeneous mixture of its constituent components to better model scattering within it. Simulation of the decay products of all of the uranium isotopes and the local geometry (table and tee) could improve the HEU computed response spectrum in the secondary peak regions.

REFERENCES

[1] J. J. Duderstadt and L. J. Hamilton, Nuclear Reactor Analysis, Ann Arbor, MI: John Wiley & Sons, 1976.

[2] W. L. Dunn and J. K. Shultis, Exploring Monte Carlo Methods, Burlington, MA: Academic Press, 2012.

[3] P. R. Bevington and K. D. Robinson, Data Reduction and Error Analysis, Boston: McGraw-Hill, 2003.

[4] R. L. Heath, "Scintillation Spectrometry Gamma-Ray Spectrum Catalogue," Idaho National Laboratories, Idaho Falls, ID, 1997.

[5] J. H. Hubbell, "Photon Cross Sections, Attenuation Coefficients, and Energy Absorption Coefficients From 10 keV to 100 GeV," National Bureau of Standards, Washington, D.C., 1969.

[6] H. Iams and B. Salzberg, "The Secondary Emission Phototube," in *Proceedings of the Institute of Radio Engineers*, New York City, 1935.

[7] G. Kelley, "Multichannel Analyzer". United States of America Patent 2642527, 16 June 1953.

[8] R. G. Lerner and G. L. Trigg, Encyclopaedia of Physics, Weinham, Germany: VCH, 1990.

[9] G. F. Knoll, Radiation Detection and Measurement, Hoboken, NJ: John Wiley & Sons, 2000.

[10] J. K. Shultis and R. E. Faw, Radiation Shielding, La Grange Park, IL: American Nuclear Society, Inc., 2000.

[11] R. C. Smith, Uncertainty Quantification, Philadelphia: Society for Industrial and Applied Mathematics, 2014.

[12] A. Sood, "A New Monte Carlo Assisted Approach to Detector Response Functions," North Carolina State University, Raleigh, NC, 2000.

[13] X.-5. M. C. Team, "MCNP-A General Monte Carlo N-Particle Transport Code, Version 5," Los Alamos National Laboratory, Los Alamos, NM, 2003.

[14] "Scintillation Detection," Florida International University, 2011. [Online]. Available: `http://wanda.fiu.edu/teaching/courses/Modern_lab_manual/scintillator.html#`. [Accessed 11 April 2014].

[15] A. Berlizov, "Help: Gamma Spectrum Generator," 10 April 2008. [Online]. Available: `http://www.nucleonica.net/wiki/index.php/Help:Gamma_Spectrum_Generator`. [Accessed 11 April 2014].

[16] R. P. Gardner and A. Sood, "A Monte Carlo simulation approach for generating NaI detector response functions (DRFs) that accounts for non-linearity and variable flat continua," *Nuclear Instruments and Methods in Physics Research B*, vol. 213, pp. 87-99, 2004.

[17] R. J. Beattie and J. Byrne, "A Monte Carlo Program for Evaluating the Response of a Scintillation Counter to Monoenergetic Gamma Rays," *Nuclear Instuments and Methods*, vol. 104, pp. 163-168, 1972.

[18] M. J. Berger and S. M. Seltzer, "Response Functions for Sodium Iodide Scintillation Detection," *Nuclear Instruments and Methods*, vol. 104, pp. 317-332, 1972.

[19] H. Haario, M. Laine and A. Mira, "DRAM: Efficient adaptive MCMC," *Stat Comput*, vol. 16, pp. 339-354, 2006.

[20] R. Hofstadter, "The Detection of Gamma-Rays with Thallium-Activated Sodium Iodide Crystals," *Physics Review*, vol. 75, p. 796, 1949.

[21] A. Owens, "Spectral Degredation Effects in an 86 cm^3 Ge(HP) Detector," *Nuclear Instruments and Methods in Physics Research A*, vol. 238, no. 2-3, pp. 473-478, 1985.

[22] D. E. Peplow, "Sodium Iodide Detector Response Functions Using Simplified Monte Carlo Simulation and Principal Components," *Nuclear Geophysics*, vol. 8, no. 3, pp. 243-259, 1994.

[23] J. Wang, Z. Wang, J. Peeples, H. Yu and R. P. Gardner, "Development of a Simple Detector Response Function Generation Program: The CEARDRFs Code," *Applied Radiation and Isotopes*, vol. 70, pp. 1166-1174, 2012.

[24] R. P. Gardner, Interviewee, *Absolute Efficiency Factor for g03*. [Interview]. 15 January 2014.

[25] M. J. Berger, J. H. Hubbell, S. M. Seltzer, J. Chang, J. S. Coursey, R. Sukumar, D. S. Zucker and K. Olsen, "XCOM: Photon Cross Sections Database," National Institute of Standards and Technology, 9 Dec. 2011. [Online]. Available: `http://www.nist.gov/pml/data/xcom/`. [Accessed 15 July 2014].

[26] R. P. Gardner, C. L. Barrett, W. Haq and D. E. Peplow, "Efficient Monte Carlo Simulation of O-16 Neutron Activation and N-16 Decay Gamma-Ray Detection in a Flowing Fluid for On-Line

Oxygen Analysis or Flow Rate Measurement," *Nuclear Science and Engineering,* vol. 122, pp. 326-343, 1996.

[27] Eckert & Ziegler Isotope Products, "Eckert & Ziegler Reference & Calibration Sources: Product Information," Valencia, CA, 2007.

[28] National Nuclear Data Center, "Nudat2.6: Decay Radiation Search," Brookhaven National Laboratory, 2013. [Online]. Available: `http://www.nndc.bnl.gov/nudat2/indx_dec.jsp`. [Accessed 14 June 2015].

APPENDIX

APPENDIX

A

ALTERNATIVE METHODS AND MODELS

This appendix contains a couple of alternative methods for parts of the validation and uncertainty quantification work, as well as an alternative model for the simulation of detector responses. The alternatives are compared with the chosen primary methods, and then the reasoning behind the method chosen is discussed briefly.

A.1   HEU Disc Response: Separate Versus Combined Peaks

At first, the number of full energy peaks chosen to be entered into g03 for simulation were only those that were over 1% in relative intensity. Seven peaks met this criteria, and so the seven peaks were matched with their relative channel locations and entered into g03. The resulting spectrum did not approximate the large lower intensity peak next to the main peak at 186 keV very well in early simulations. This peak was the result of the interaction between three full energy peaks: one at 144, 163, and the 186 keV peak.

It was thought that combining the two lower energy and intensity peaks may improve the result. So, their energies were averaged to 150 keV and their intensities summed before entering them into g03, leaving only six peaks. A comparison of the two responses for the HEU disc case centered at forty one centimeters from the detector is shown in Figure A.1.
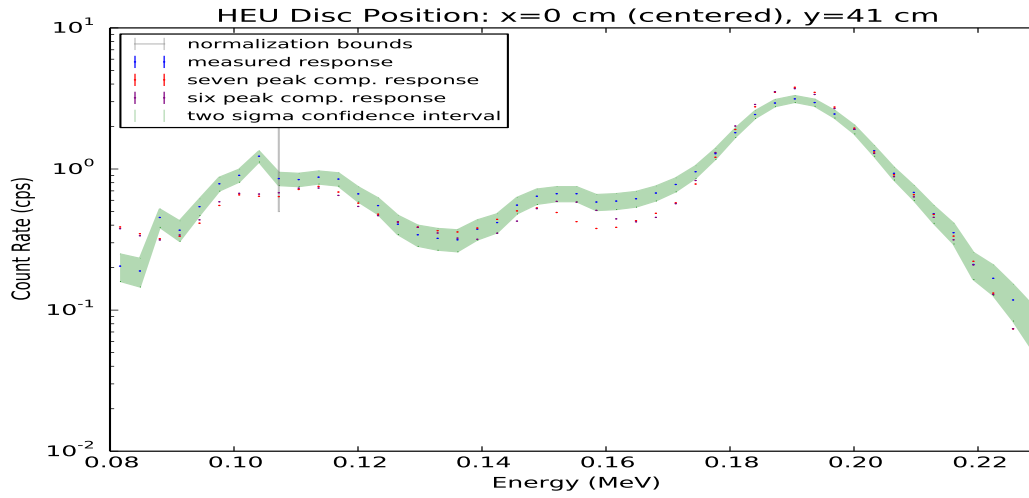
Figure A.1 Full simulation of seven peaks vs. six peaks with two combined at 150 keV.

Both responses underestimate the lower energy peaks while slightly overestimating the main full energy peak at 186 keV. Note: this was a low number of histories run, so the added uncertainty in the calculation made the 100 keV peaks appear closer to the lead backscatter peaks. In the high fidelity runs, the underestimation of the backscatter peaks is more apparent.

It is clear though that the combined peak aligns much better with the center of the peak around 150 keV and more closely approximates its amplitude. As a consequence of this result, the six peak scheme was chosen for the final results.

A.2   Freqentist and Bayesian Power Law Uncertainty

In the main body of this work, it was mentioned that Frequentist uncertainty analysis was performed on the power law model due to the lack of confidence in the Bayesian code's ability to analyze the weighted least squares scheme. Later, the Bayesian code was tested and compared with the Frequentist calculation. The results of both analyses for the power law parameters are contained in Table A.1.

Table A.1 Power law parameter means and standard deviations for Frequentist and Bayesian methods.

Frequentist				
Parameter	Mean	Standard Deviation, σ	Relative STD, σ_{rel} (%)	χ^2_ν
a	0.027608	1.684E-4	0.6100	8.500E-6
b	0.644237	5.719E-3	0.8877	
Bayes				
a	0.027608	1.606E-4	5.818E-3	8.501E-6
b	0.64436	5.75E-3	8.923E-3	

The values of the parameters and their respective uncertainties are very similar for both methods. The Bayesian parameters gain a slightly less overfit reduced chi-squared value, and exchange slightly lower uncertainty in a for greater uncertainty in b. Again, the Frequentist method was chosen for expedience and direct application of the weighted least squares, however, the methods prove to be essentially equivalent in this case.

A.3   Alternative Response Calculation: MCNP F8 Tally

Gardner's DRF model proved to be able to simulate the full energy peaks of responses fairly well, but needs recalibration for some detectors to reproduce good Compton continua. Additionally it suffers under the strain of advanced geometries being unable to reproduce the effects of outside detector scattering events on the detector response. One alternative model was considered and compared to g03 responses: MCNP's F8 tally with Gaussian energy broadening (GEB).

MCNP can approximate a detector response to a fair degree with the correct geometry. The same detector and source model as was used for the the F4 flux tally was used for the F8 tally. Additionally the power law equation for MCNP (Equation A.1) was fit to the same sources used for Gardner's model

$$f whm = a + b\sqrt{E + cE^2} \tag{A.1}$$

where E is the energy of the incident gamma ray, a,b and c the parameters, and fwhm is the full width at half maximum of the peak. This information was used in a special GEB input of the F8 tally in order to spread the peak to the appropriate width in the resulting response from MCNP. The response from MCNP is compared with the response created by g03 and the experimental response in Figure A.2
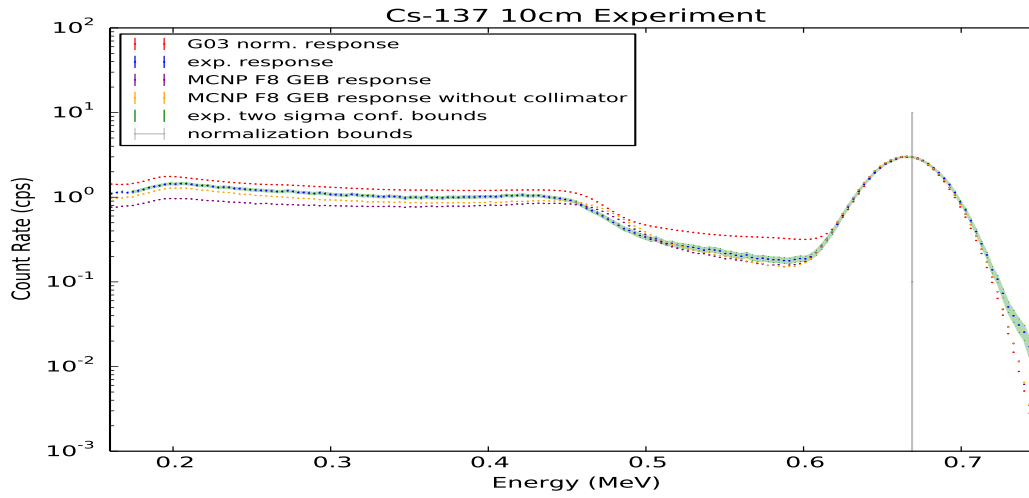
71

Figure A.2 Peak normalized computed responses from MCNP with and without the collimator simulated and g03 versus the measured response.

Both methods approximate the full-energy peak well, however, where g03 overestimates the continuum MCNP underestimates. MCNP predicts the electron physics of the valley region better than g03 (without recalibration of the range law), but underestimates the rest of the Compton continuum by a good margin. The response from MCNP without the collimator is shown to illustrate a possible cause of they underestimation. There is a great shift in the continuum without the lead, so it seems likely that some physics with the lead collimator and aluminum can of the detector are not well approximated by MCNP's F8 tally.

g03 was chosen as the main model mainly for two reasons. First, g03 calculates a DRF with far fewer histories (four orders of magnitude) with similar accuracy and thereby taking much less time for computation. Second, g03 produces a full DRF for the user which will be useful in further research with inverse problems, whereas MCNP produces a response directly without a DRF. However, it may still be useful to give the MCNP calculation a closer examination for its approximations of the physics in the valley region in order to improve future models.